The Astronomical Journal, 167:269 (30pp), 2024 June https://doi.org/10.3847/1538-3881/ad3ba3

Systematic KMTNet Planetary Anomaly Search. XI. Complete Sample of 2016 Subprime Field Planets

In-Gu Shin[1], Jennifer C. Yee[1], Weicheng Zang[1,2], Cheongho Han[3], Hongjing Yang[2], Andrew Gould[4,5], Chung-Uk Lee[6], Andrzej Udalski[7], Takahiro Sumi[8]
(Leading authors),
Michael D. Albrow[9], Sun-Ju Chung[6], Kyu-Ha Hwang[6], Youn Kil Jung[6,10], Yoon-Hyun Ryu[6], Yossi Shvartzvald[11], Sang-Mok Cha[6,12], Dong-Jin Kim[6], Hyoun-Woo Kim[6], Seung-Lee Kim[6], Dong-Joo Lee[6], Yongseok Lee[6,12], Byeong-Gon Park[6], Richard W. Pogge[5]
(The KMTNet Collaboration),
Przemek Mróz[7], Michał K. Szymański[7], Jan Skowron[7], Radosław Poleski[7], Igor Soszyński[7], Paweł Pietrukowicz[7], Szymon Kozłowski[7], Krzysztof A. Rybicki[11,7], Patryk Iwanek[7], Krzysztof Ulaczyk[13], Marcin Wrona[7], Mariusz Gromadzki[7]
(The OGLE Collaboration),
and
Fumio Abe[14], Ken Bando[8], Richard Barry[15], David P. Bennett[15,16], Aparna Bhattacharya[15,16], Ian A. Bond[17], Hirosane Fujii[14], Akihiko Fukui[18,19], Ryusei Hamada[8], Shunya Hamada[8], Naoto Hamasaki[8], Yuki Hirao[20], Stela Ishitani Silva[15,21], Yoshitaka Itow[14], Rintaro Kirikawa[8], Naoki Koshimoto[8], Yutaka Matsubara[14], Shota Miyazaki[22], Yasushi Muraki[14], Tutumi Nagai[8], Kansuke Nunota[8], Greg Olmschenk[15], Clément Ranc[23], Nicholas J. Rattenbury[24], Yuki Satoh[8], Daisuke Suzuki[8], Mio Tomoyoshi[8], Paul. J. Tristram[25], Aikaterini Vandorou[15,16], Hibiki Yama[8], and Kansuke Yamashita[8]
(The MOA Collaboration)

[1] Center for Astrophysics, Center for Astrophysics | Harvard & Smithsonian, 60 Garden Street, Cambridge, MA 02138, USA
[2] Department of Astronomy, Tsinghua University, Beijing 100084, People's Republic of China
[3] Department of Physics, Chungbuk National University, Cheongju 28644, Republic of Korea
[4] Max Planck Institute for Astronomy, Königstuhl 17, D-69117 Heidelberg, Germany
[5] Department of Astronomy, The Ohio State University, 140 W. 18th Avenue, Columbus, OH 43210, USA
[6] Korea Astronomy and Space Science Institute, Daejeon 34055, Republic of Korea
[7] Astronomical Observatory, University of Warsaw, Al. Ujazdowskie 4, 00-478 Warszawa, Poland
[8] Department of Earth and Space Science, Graduate School of Science, Osaka University, Toyonaka, Osaka 560-0043, Japan
[9] University of Canterbury, Department of Physics and Astronomy, Private Bag 4800, Christchurch 8020, New Zealand
[10] Korea University of Science and Technology (UST), 217 Gajeong-ro, Yuseong-gu, Daejeon 34113, Republic of Korea
[11] Department of Particle Physics and Astrophysics, Weizmann Institute of Science, Rehovot 76100, Israel
[12] School of Space Research, Kyung Hee University, Yongin, Kyeonggi 17104, Republic of Korea
[13] Department of Physics, University of Warwick, Gibbet Hill Road, Coventry, CV4 7AL, UK
[14] Institute for Space-Earth Environmental Research, Nagoya University, Nagoya 464-8601, Japan
[15] Code 667, NASA Goddard Space Flight Center, Greenbelt, MD 20771, USA
[16] Department of Astronomy, University of Maryland, College Park, MD 20742, USA
[17] Institute of Natural and Mathematical Sciences, Massey University, Auckland 0745, New Zealand
[18] Department of Earth and Planetary Science, Graduate School of Science, The University of Tokyo, 7-3-1 Hongo, Bunkyo-ku, Tokyo 113-0033, Japan
[19] Instituto de Astrofísica de Canarias, Vía Láctea s/n, E-38205 La Laguna, Tenerife, Spain
[20] Institute of Astronomy, Graduate School of Science, The University of Tokyo, 2-21-1 Osawa, Mitaka, Tokyo 181-0015, Japan
[21] Department of Physics, The Catholic University of America, Washington, DC 20064, USA
[22] Institute of Space and Astronautical Science, Japan Aerospace Exploration Agency, 3-1-1 Yoshinodai, Chuo, Sagamihara, Kanagawa 252-5210, Japan
[23] Sorbonne Université, CNRS, UMR 7095, Institut d'Astrophysique de Paris, 98 bis bd Arago, 75014 Paris, France
[24] Department of Physics, University of Auckland, Private Bag 92019, Auckland, New Zealand
[25] University of Canterbury Mt. John Observatory, P.O. Box 56, Lake Tekapo 8770, New Zealand
Received 2024 January 8; revised 2024 April 2; accepted 2024 April 6; published 2024 May 16

Abstract

Following Shin et al. (2023b), which is a part of the "Systematic KMTNet Planetary Anomaly Search" series (i.e., a search for planets in the 2016 KMTNet prime fields), we conduct a systematic search of the 2016 KMTNet subprime fields using a semi-machine-based algorithm to identify hidden anomalous events missed by the conventional by-eye search. We find four new planets and seven planet candidates that were buried in the KMTNet archive. The new planets are OGLE-2016-BLG-1598Lb, OGLE-2016-BLG-1800Lb, MOA-2016-BLG-526Lb, and KMT-2016-BLG-2321Lb, which show typical properties of microlensing planets, i.e., giant planets orbit M-dwarf host stars beyond their snow lines. For the planet candidates, we find planet/binary or 2L1S/1L2S degeneracies, which are an obstacle to firmly claiming planet detections. By combining the results of Shin et al. (2023b) and this work, we find a total of

nine hidden planets, which is about half the number of planets discovered by eye in 2016. With this work, we have met the goal of the systematic search series for 2016, which is to build a complete microlensing planet sample. We also show that our systematic searches significantly contribute to completing the planet sample, especially for planet/host mass ratios smaller than 10^{-3}, which were incomplete in previous by-eye searches of the KMTNet archive.

Unified Astronomy Thesaurus concepts: Gravitational microlensing exoplanet detection (2147)

1. Introduction

Since 2016, the Korea Microlensing Telescope Network (KMTNet; Kim et al. 2016) has operated a microlensing survey to detect exoplanets using their near-continuous observations toward the Galactic bulge. As of 2023, the KMTNet has contributed to the discovery/characterization of more than 135 microlensing planets.[26] Initially, the planetary events were identified by a traditional method, i.e., "by-eye" search.

The human dependence of that method, which relies on the experience or insight of operators, is difficult to quantify, and there may exist missing or hidden planets. Thus, we conduct a series of works called "Systematic KMTNet Planetary Anomaly Search" to find *hidden* planets in the KMTNet data archive in order to build a complete microlensing planet sample. The complete sample can be used to construct well-defined samples of planets for statistical studies such as the planet frequency and mass-ratio distribution of planetary systems in our Galaxy.

To systematically search anomalous events in the KMTNet data archive, we use a semi-machine-based algorithm called AnomalyFinder (AF; Zang et al. 2021, 2022) instead of the by-eye search. The AF search is separately conducted for each year and cadence. The nominal cadences of the KMTNet observations have two categories, which are high cadence ($\Gamma = 2.0$–$4.0\,\mathrm{hr}^{-1}$ for prime fields) and low cadence ($\Gamma = 0.2$–$1.0\,\mathrm{hr}^{-1}$ for subprime fields). The detailed information of the KMTNet fields is described in Kim et al. (2018).

Based on the AF searches, we conducted detailed light-curve analyses for the identified anomalous events. The parts of this AF series have been published or submitted. Indeed, from the systematic search, we can find hidden planets that are missing from the by-eye search. Shin et al. (2023b) reported five planets, which were newly found in the 2016 prime fields. Ryu et al. (2024) report three new planets found in the 2017 prime fields.[27] Gould et al. (2022), Wang et al. (2022), and Hwang et al. (2022) reported a total of 12 new planets, which were discovered in the 2018 prime fields. Jung et al. (2022) reported six new planets found in the 2018 subprime fields. Zang et al. (2021, 2022) and Hwang et al. (2022) reported a total of seven new planets discovered in the 2019 prime fields. Jung et al. (2023) reported five new planets found in the 2019 subprime fields. Lastly, Zang et al. (2023) present seven new planets having $q < 10^{-4}$, which were identified by the AF in the KMTNet data archive observed from 2016 to 2019. Although our systematic search works are not complete, yet, we have found a total of 45 hidden planets in the KMTNet archive, which amounts to about 33% of the total microlensing planets discovered from 2016 to 2022.

Following the work of Shin et al. (2023b), we conduct the AF search for 2016 subprime fields to find hidden planetary systems. The AF identifies a total of 113 anomalous events in the fields, including the recovery of all previously published planetary events identified by eye (i.e., eight events). Among them, we find that 83 events were caused by binary-lens systems (i.e., $q > 0.06$) from the preliminary light-curve analyses using the KMTNet pipeline data. For the remaining 22 events, we conduct detailed light-curve analyses using the rereduced data sets with the best quality (see Section 2). The detailed analyses reveal that 11 events do not have possible planetary solutions (i.e., $q < 0.03$; see Appendix). Finally, we find four new planetary events and seven planet candidates on the 2016 subprime fields. The new planets are OGLE-2016-BLG-1598Lb, OGLE-2016-BLG-1800Lb, MOA-2016-BLG-526Lb, and KMT-2016-BLG-2321Lb. We present the detailed light-curve analyses for these planetary events in Section 3. In this section, we also present the analyses of the planet candidates to show the possibility of planet detection. In Sections 4 and 5, we present the analyses of color–magnitude diagrams (CMDs) and lens properties of each planetary system, respectively. Lastly, we summarize our findings in Section 6.

2. Observations

Although the AF identified anomalous events based on the KMTNet data archive, these events may also have been independently observed or discovered by other microlensing surveys. Thus, we gather all available data sets for each event. In Table 1, we list anomalous events that have at least one solution with $q < 0.06$ from the preliminary analyses along with their observational information. Note that, following the standard convention, we designate them according to the survey that first announced the event.

The KMTNet data sets were obtained from three identical 1.6 m telescopes equipped with 4 deg^2 wide field cameras, which are located at three sites in the Southern Hemisphere, i.e., the Cerro Tololo Inter-American Observatory in Chile (KMTC), South African Astronomical Observatory in South Africa (KMTS), and Siding Spring Observatory in Australia (KMTA). Note that, in the figures, the two-digit number after the site acronym indicates the field number of the KMTNet survey. These sites cover well-separated time zones to achieve near-continuous observations. The KMTNet observations are initially reduced using their pySIS pipeline (Albrow et al. 2009), which adopts the difference image analysis (DIA) method (Tomaney & Crotts 1996; Alard & Lupton 1998). For KMTC and KMTS observations, the KMTNet survey regularly takes one *V*-band observation for every 10th and 20th *I*-band observations, respectively (Johnson-Cousins *BVRI* filter system). The pipeline data are available at the KMTNet alert system (Kim et al. 2018).[28]

Note that we manually rereduced the KMTNet data sets for each preliminary planet candidate listed in Table 1 using the

[26] We count the discovered microlensing planets using the NASA Exoplanet Archive (https://exoplanetarchive.ipac.caltech.edu/) as of 2023 October.

[27] Among the three planetary events, two events were newly identified by the AF. While one event was previously identified by eye, however, this event was not published due to technical complications.

[28] https://kmtnet.kasi.re.kr/ulens/

Table 1
Observations of 2016 Planets and Planet Candidates

Event			Location			Obs. Info.	
KMTNet	OGLE	MOA	R.A. (J2000)	decl. (J2000)	(ℓ, b)	A_I	Γ (hr^{-1})
0696	**1598**	521	$18^h00^m45^s.78$	$-29°10'31''.58$	$(+1.^\circ47, -2.^\circ97)$	1.16	1.0
0781	**1800**	581	$17^h59^m36^s.77$	$-30°51'55''.30$	$(-0.^\circ12, -3.^\circ59)$	1.72	1.0
1611	1705	**526**	$17^h46^m40^s.39$	$-34°23'09''.89$	$(-4.^\circ54, -3.^\circ02)$	1.50	0.4
2321	···	···	$17^h36^m13^s.90$	$-25°31'29''.57$	$(+1.^\circ79, +3.^\circ58)$	3.88	0.4
1243	···	···	$17^h49^m55^s.56$	$-22°11'57''.91$	$(+6.^\circ27, +2.^\circ65)$	1.98	0.4
1406	**0336**	092	$18^h16^m09^s.86$	$-25°08'02''.29$	$(+6.^\circ68, -4.^\circ02)$	1.18	0.4
1449	**0882**	···	$18^h14^m50^s.42$	$-27°40'06''.71$	$(+4.^\circ29, -4.^\circ96)$	0.52	0.4
1609	**1704**	···	$17^h47^m32^s.79$	$-34°42'40''.10$	$(-4.^\circ73, -3.^\circ34)$	1.04	0.4
1630	**1408**	···	$17^h40^m38^s.76$	$-35°55'51''.96$	$(-6.^\circ51, -2.^\circ78)$	2.33	0.4
2399	···	···	$17^h42^m13^s.00$	$-22°56'15''.14$	$(+4.^\circ72, +3.^\circ79)$	1.76	0.4
2473	···	···	$17^h41^m24^s.88$	$-32°21'32''.40$	$(-3.^\circ39, -1.^\circ03)$	4.93	1.0
0255	**0620**	183	$18^h11^m21^s.81$	$-26°50'24''.11$	$(+4.^\circ66, -3.^\circ88)$	1.06	0.4
0913	···	···	$17^h35^m43^s.08$	$-29°12'14''.87$	$(-1.^\circ37, +1.^\circ69)$	3.02	1.0
1004	**1432**	···	$17^h34^m01^s.67$	$-26°56'02''.98$	$(+0.^\circ34, +3.^\circ23)$	2.41	1.0
1222	···	···	$17^h44^m29^s.20$	$-24°43'38''.10$	$(+3.^\circ46, +2.^\circ41)$	2.89	1.0
1326	**1844**	···	$17^h59^m12^s.49$	$-33°10'20''.78$	$(-2.^\circ17, -4.^\circ66)$	1.42	1.4
1425	···	···	$18^h11^m30^s.35$	$-26°38'02''.62$	$(+4.^\circ85, -3.^\circ81)$	1.03	0.4
1433	**0982**	···	$18^h09^m56^s.99$	$-26°45'28''.01$	$(+4.^\circ58, -3.^\circ57)$	1.35	0.4
1461	**1517**	···	$18^h13^m49^s.10$	$-28°24'48''.60$	$(+3.^\circ53, -5.^\circ11)$	0.43	0.4
2067	**1258**	···	$17^h44^m15^s.45$	$-26°31'13''.73$	$(+1.^\circ90, +1.^\circ52)$	3.18	1.0
2256	···	···	$17^h36^m36^s.13$	$-25°59'10''.61$	$(+1.^\circ45, +3.^\circ26)$	2.98	1.0
2331	···	···	$17^h43^m39^s.02$	$-26°07'51''.31$	$(+2.^\circ16, +1.^\circ84)$	2.87	1.0

Note. The boldface indicates the "discovery" name of each event. The horizontal lines separate planetary events, planet candidates, and nonplanetary events (see Appendix).

updated pySIS package described in Yang et al. (2024). We conduct light-curve analyses based on these tender-loving-care (TLC) reductions, which have checked the anomalous data points with the best quality.

The Optical Gravitational Lensing Experiment (OGLE; Udalski et al. 2015) data sets were obtained from a 1.6 m Warsaw telescope equipped with a 1.4 deg^2 field camera, which is located at Las Campanas Observatory in Chile. For the OGLE observations, it mainly takes *I*-band observations and periodically takes *V*-band observations. The OGLE observations are reduced by their own DIA pipeline (Wozniak 2000). The data are available on the OGLE Early Warning System (Udalski et al. 1994).[29]

The Microlensing Observations in Astrophysics (MOA; Bond et al. 2001; Sumi et al. 2003) data sets were obtained from a 1.8 m telescope located at Mt. John University Observatory in New Zealand. The observations were made in the MOA red band (hereafter, referred to as *R* band), which has wavelength ranges of 609–1109 nm and transmission ranges of 0.0–0.978 (i.e., a rough sum of the Cousins *R* and *I* bands). The MOA observations were reduced by their DIA pipeline (Bond et al. 2001), which are available on the MOA alert system.[30]

3. Light-curve Analysis

3.1. Basics of the Light-curve Analysis

We conduct the light-curve analysis following the procedures described in Shin et al. (2023b), which describes the systematic KMTNet planetary anomaly search for 2016 prime-field events. To avoid redundant descriptions for analysis procedures, we do not present the details here. However, in Table 2, we present definitions of acronyms and model parameters to describe the analysis results in the following sections. For each event, we conduct the heuristic analysis described in Ryu et al. (2022) to predict s and/or q values (also, to guess its possible degeneracy).[31] We note that we test the APRX effect if the event has a relatively long timescale, which is defined as larger than $t_E > 15.0$ days. Once we detect the APRX effect, we also test the OBT effect and xallarap effect to confirm the robustness of the APRX detection. Because the OBT can affect the APRX measurement and its uncertainty, and the xallarap can mimic the APRX effect. Lastly, if we find a planetary solution(s) from bump-shaped anomalies on the light curve, we test the 2L1S/1L2S degeneracy (Gaudi 1998) to confirm planet detection. To quantitatively compare various models for each event based on the $\Delta\chi^2$, we rescale the errors of each data set based on the best-fit solution using the method described in Yee et al. (2012). The error rescaling process can make each data point contribute $\chi^2 \sim 1$.

3.2. Planetary Events

We find four events caused by planetary lens systems that satisfy our minimum criteria to claim planet detection. For clarity, we summarize our criteria to claim planet detection as follows:

[29] https://ogle.astrouw.edu.pl/ogle4/ews/ews.html
[30] https://www.massey.ac.nz/~iabond/moa/alerts/
[31] For the details of the heuristic analysis, the heuristic analysis was originally introduced in Hwang et al. (2022). The formalism was modified for better approximation, which is described in Gould et al. (2022). Ryu et al. (2022) presented a unified formalism of the analysis.

Table 2
Definition of Acronyms and Model Parameters

Acronym	Definition
nLmS	Number of lenses (n) and sources (m), which are included for models
STD[a]	Static model without any consideration of acceleration for the lens, source, and observer
APRX	Model considering the annual microlens-parallax (APRX) effect (Gould 1992)
OBT	Model considering the effect of the orbital motion (OBT) of lens system
Model parameter	**Definition**
t_0	Time at the peak of the light curve
u_0	Impact parameter in units of $\theta_{\rm E}$
$t_{\rm E}$	Time during which the source travels the angular Einstein ring radius ($\theta_{\rm E}$)
s	Projected separation between lens components in units of $\theta_{\rm E}$
q	Mass ratio of the lens components defined as $q \equiv M_{\rm secondary}/M_{\rm primary}$
α	Angle of the source trajectory with respect to the binary axis of lens components (e.g., 0 is toward the planet or π is toward the host if $q < 1$)
ρ_*	Angular source radius (θ_*) scaled by $\theta_{\rm E}$, i.e., $\rho_* \equiv \theta_*/\theta_{\rm E}$
$t_{0,{\rm Sm}}$ ($m = 1, 2$)	Times of closest approach to the lens by the first and second sources, respectively
$u_{0,{\rm Sm}}$ ($m = 1, 2$)	Impact parameter between the lens and the first and second sources, respectively
$q_{\rm flux}$	Flux (f) ratio of the binary sources defined as $q_{\rm flux} \equiv f_{\rm S2}/f_{\rm S1}$
s_n ($n = 1, 2$)	Projected separations between lens components, i.e., s_n indicates the separation between m_1 and $m_{(n+1)}$ where $n = 1, 2$
q_n ($n = 1, 2$)	Mass ratios of the lens components defined as $q_n \equiv m_{(n+1)}/m_1$
ψ	Orientation angle of m_3 measured from the $m_1 - m_2$ axis with the m_1 origin
$\pi_{{\rm E},E}$	East component of the microlens-parallax vector, $\boldsymbol{\pi}_{\rm E} \equiv (\pi_{{\rm E},N}, \pi_{{\rm E},E})$, projected on the sky
$\pi_{{\rm E},N}$	North component of the $\boldsymbol{\pi}_{\rm E}$
ds/dt	Changes of s in time (year) caused by the orbital motion of the lens system
$d\alpha/dt$	Changes of α in time (year)

Note.
[a] We conduct modeling using the static case as the standard (STD) model.

(a) The mass ratio of the best-fit planetary solution must be smaller than 0.03 (i.e., $q < 0.03$).
(b) Competing binary-lens solutions can be resolved by $\Delta\chi^2 > 10.0$.
(c) If the 2L1S/1L2S degeneracy exists, 1L2S can be resolved by $\Delta\chi^2 > 15.0$.

These are the criteria used in other works and for the construction of the statistical sample in Zang et al. (2024). They are somewhat arbitrary, but for the construction of a statistical sample, the most important thing is that they can be incorporated into a sensitivity analysis in a straightforward way. In addition, we provide sufficient information on each event to allow a different choice of criteria. We present the details of the light-curve analysis for each planetary event in the following sections.

3.2.1. OGLE-2016-BLG-1598

As shown in Figure 1, the light curve of OGLE-2016-BLG-1598 (which we identified as KMT-2016-BLG-0696) exhibits a shallow-dip anomaly near the peak (i.e., HJD′ = 7636.0 ∼ 7639.0), which shows clear residuals from the 1L1S model (i.e., $\Delta\chi^2_{\rm 1L1S-2L1S} = 171.9$). The anomaly can be explained by two 2L1S models caused by the inner/outer degeneracy. Although the degenerate models cannot be resolved (i.e., $\Delta\chi^2 = 8.5$), both cases indicate that the lens system is a planetary system (i.e., $q < 0.03$) as presented in Table 3. Thus, we conclude that OGLE-2016-BLG-1598 was caused by a planetary lens system. Indeed, the heuristic analysis ($t_{\rm anom} = 7637.5$, $\tau_{\rm anom} = -0.1045$, and $u_{\rm anom} = 0.2436$) predicts $s^\dagger_- = 0.886$, $s^\dagger_+ = 1.129$, and $q \sim 6.4 \times 10^{-4}$. The predicted q is consistent with the empirical $q = 6.44 \times 10^{-4}$ value. Also, the empirical $s^\dagger = \sqrt{s_{\rm inner}\, s_{\rm outer}} = 0.833$ is similar to the predicted $s^\dagger_-$ value.

Because of the relatively long timescale ($t_{\rm E} \sim 38$ days) for all cases, we test the annual APRX effect. As shown in Figure 2, we find the χ^2 improves by ∼20.7 when we consider the APRX effect, which mostly comes from the OGLE data. However, the improvement of the OGLE data is inconsistent with the KMTNet and MOA data. Moreover, there is no improvement in the case of the KMTC data although the KMTC data have similar coverage to the OGLE data. Thus, we separately conduct APRX modeling using KMTC and OGLE only. We find that the OGLE-only case favors too large APRX values (i.e., $|\boldsymbol{\pi}_{\rm E}| > 2.82$), which are unreliable. In contrast, the KMTC-only case shows that the APRX values are consistent with a nondetection (i.e., $(\pi_{{\rm E},E}, \pi_{{\rm E},N}) \sim (0.0, 0.0)$ within 1σ level). The inconsistency between OGLE and KMTNet data of both the χ^2 improvements and the APRX measurements indicates that the APRX effect of this event is unreliable. We test again the APRX effect using rereduced OGLE data. Even though we use the best-quality data sets, we have the same results from the test. Hence, we conclude that the STD models should be the fiducial solutions for this event.

3.2.2. OGLE-2016-BLG-1800

In Figure 3, we present the light curve of OGLE-2016-BLG-1800 (which we identified as KMT-2016-BLG-0781), which shows deviations (HJD′ = 7651.0–7657.0) from the 1L1S model. The anomaly can be explained by the 2L1S models that fit better by $\Delta\chi^2 = 196.33$ compared to the 1L1S fits. In Table 4, we present the model parameters of the 2L1S solutions. Indeed, the heuristic analysis predicts $s^\dagger_- = 0.918$

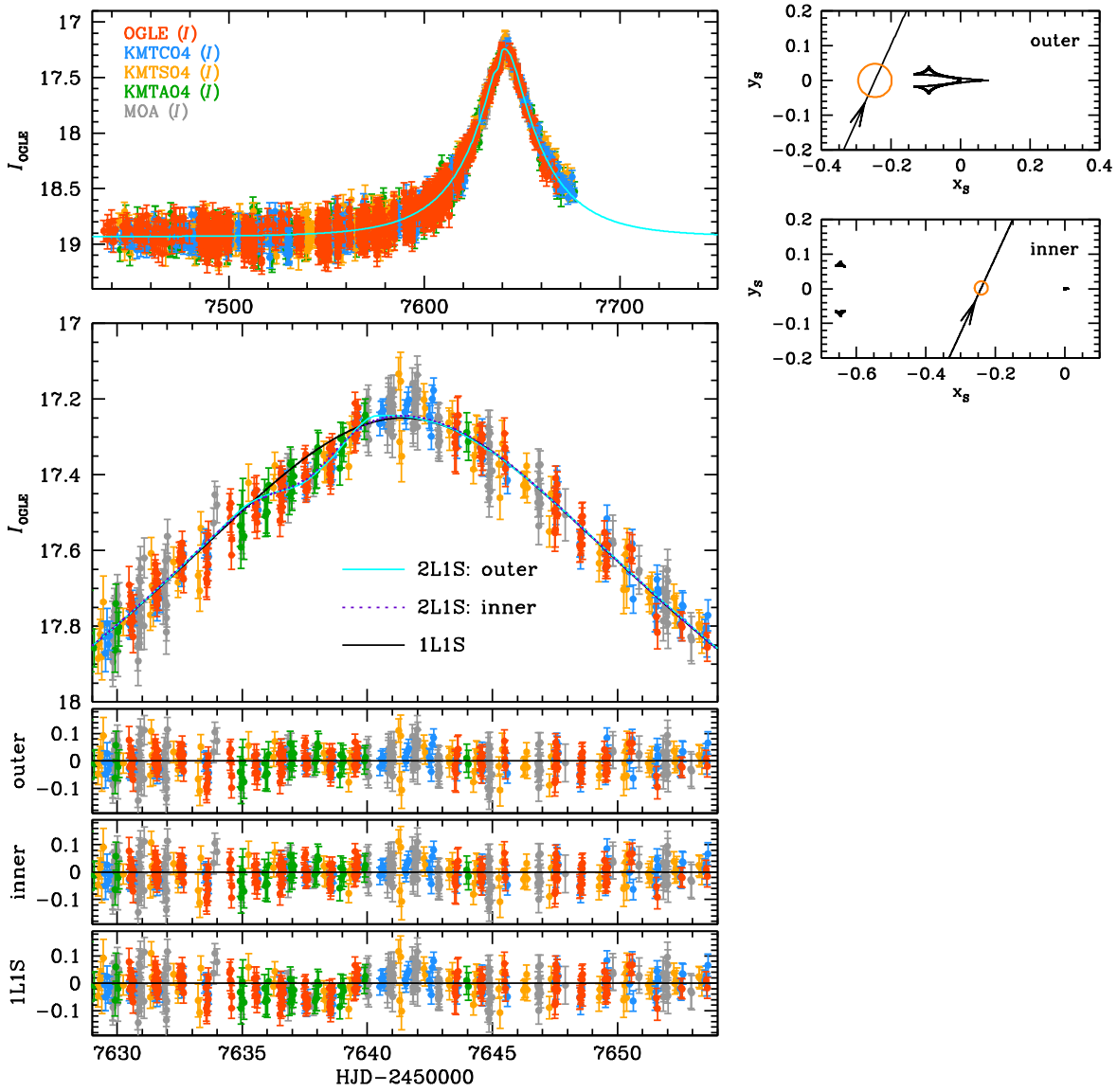

Figure 1. Light curve of OGLE-2016-BLG-1598 with 2L1S and 1L1S models. We also present caustic geometries of the 2L1S models.

Table 3
The Parameters of Degenerate 2L1S Models for OGLE-2016-BLG-1598

Parameter	Outer	Inner
$\chi^2/N_{\rm data}$	4393.288/4395	4401.751/4395
$\Delta\chi^2$	⋯ (best fit)	8.463
t_0 [HJD′]	7641.470 ± 0.037	7641.471 ± 0.035
u_0	0.225 ± 0.007	0.219 ± 0.007
$t_{\rm E}$ [days]	37.513 ± 0.810	37.833 ± 0.814
s	0.955 ± 0.057	0.727 ± 0.030
q ($\times 10^{-4}$)	6.437 ± 3.738	12.211 ± 3.543
$\langle \log_{10} q \rangle$	-3.003 ± 0.152	-2.943 ± 0.131
α [rad]	5.137 ± 0.019	5.145 ± 0.016
$\rho_{*,\rm limit}$	<0.083	<0.059

Note. HJD′ = HJD−2,450,000.0. We note that the ρ_* is not measured. Thus, we present 3σ upper limits on the ρ_* values (i.e., $\rho_{*,\rm limit}$).

and $s_+^\dagger = 1.090$ from $\tau_{\rm anom} = -0.100$, $u_{\rm anom} = 0.172$, which is similar to the value of $s^\dagger = \sqrt{s_- s_+} = 0.911$ from the models.

We find that the $s_\pm$ cases of the 2L1S solutions cannot be resolved ($\Delta\chi^2 = 0.92$). However, the mass ratios of both solutions indicate that the lens system consists of a planet and a host star. Thus, we conclude that OGLE-2016-BLG-1800 was caused by the planetary lens system.

Because the timescales of both cases are relatively long (i.e., $t_{\rm E} \sim 20$ days), we test the APRX effect for this event. However, we find the χ^2 improvement is negligible, only $\Delta\chi^2 = 0.74$. Thus, we treat the STD cases as the fiducial solutions for this event. Also, for both cases, the ρ_* is not measured as expected from the non-caustic-crossing geometries (see geometries in Figure 3).

3.2.3. MOA-2016-BLG-526

As shown in Figure 4, in the light curve of MOA-2016-BLG-526 (which we identified as KMT-2016-BLG-1611), two KMTC points near the peak exhibit an anomaly from the 1L1S model.[32] Based on the TLC reductions, we investigate these

[32] We note that MOA data did not cover the anomaly part although the MOA first announced this event. Also, the data have systematics that might be caused by the faintness of the source or bad weather conditions. Thus, we do not include the MOA data in the analysis.

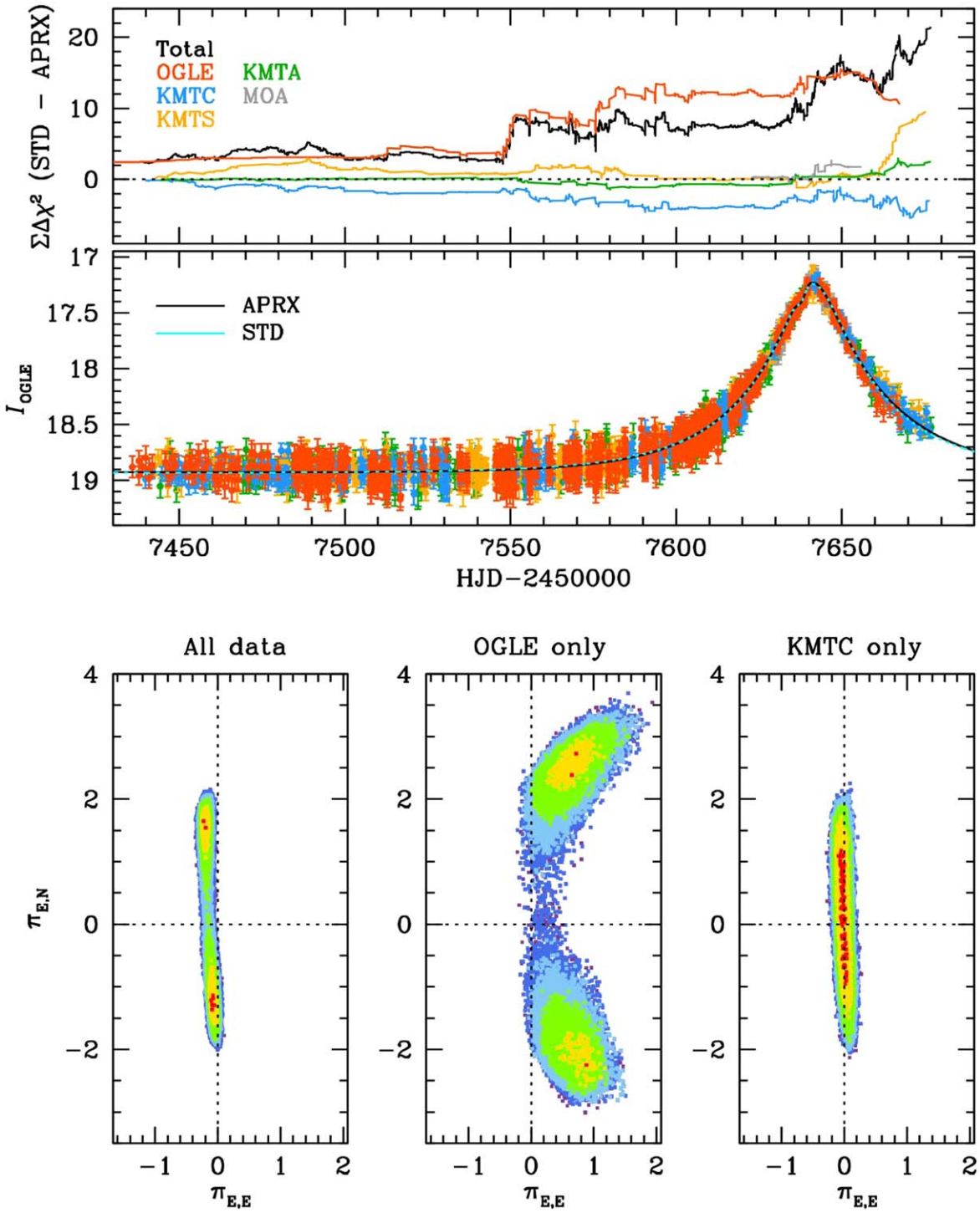

Figure 2. APRX test of OGLE-2016-BLG-1598. The upper two panels show the cumulative $\Delta\chi^2$ plot between the APRX and STD models with the light curve. The lower three panels show APRX contours obtained using all data (left), OGLE only (middle), and KMTC only (right), respectively.

points to check whether or not the anomaly is reliable. We find that the anomalous points have "normal" photometric properties compared to the average photometric properties of this event. Quantitatively, the FWHM values are 3.12 and 3.22, respectively, which are better than the average FHWM value (i.e., 3.59). The background levels of the two points are 1190.7 and 999.4, respectively. These are also better than the average value (i.e., 1370.4; we removed points that were observed during full moon phases for this average). In addition, while the photometric properties of the two points are better than average, they are also not extreme. We also visually inspected the images to confirm that there is nothing unusual about them. Hence, we conclude that the anomalous points are robust. Thus, we conduct the 2L1S modeling to describe the anomaly. We find that the 2L1S models can perfectly explain the anomaly, which shows better fits by $\Delta\chi^2 \sim 84$ compared to the 1L1S model. Moreover, although the coverage of the anomaly is sparse, as we will show below, we find that all nonplanetary

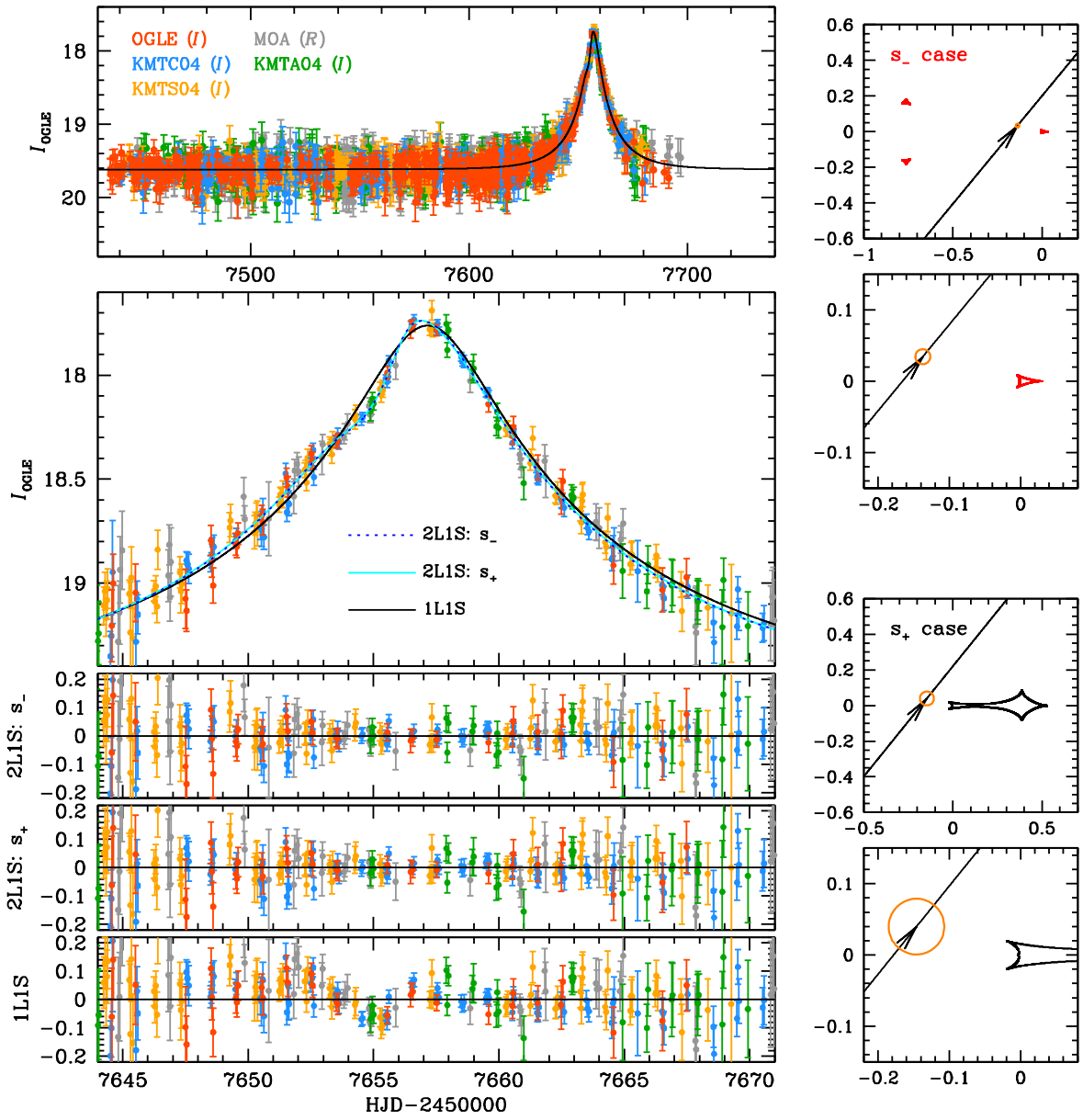

Figure 3. Light curve of OGLE-2016-BLG-1800 with both 2L1S solutions compared to the 1L1S models.

Table 4
The Parameters of 2L1S Solutions for OGLE-2016-BLG-1800

Parameter	s_-	s_+
$\chi^2/N_{\rm data}$	6117.000/6145	6117.919/6145
$\Delta\chi^2$	⋯ (best fit)	0.919
t_0 [HJD′]	7657.025 ± 0.026	7656.985 ± 0.030
u_0	0.128 ± 0.007	0.139 ± 0.009
$t_{\rm E}$ [days]	20.415 ± 0.847	19.844 ± 0.878
s	0.686 ± 0.030	1.211 ± 0.066
q ($\times 10^{-4}$)	57.528 ± 14.341	65.310 ± 23.391
$\langle \log_{10} q \rangle$	-2.229 ± 0.104	-2.133 ± 0.134
α [rad]	5.403 ± 0.016	5.392 ± 0.016
$\rho_{*,\rm limit}$	<0.057	<0.071

Note. HJD′ = HJD−2,450,000.0. We note that the ρ_* is not measured for both 2L1S cases. We present 3σ upper limits on the ρ_* values (i.e., $\rho_{*,\rm limit}$).

cases (i.e., cases having $\log_{10}(q) > -2.0$) are disfavored by 6σ level. Hence, only planetary solutions can explain the "reliable anomaly" on the light curve.

Because of the sparse coverage, we find that there exist several degenerate solutions as presented in Table 5. Indeed, we predict $s_-^\dagger = 0.954$, $s_+^\dagger = 1.048$, and $q \sim 2.9 \times 10^{-4}$ from the heuristic analysis ($\tau_{\rm anom} = -0.026$, and $u_{\rm anom} = 0.094$). The $s_-^\dagger$ is consistent with the $s^\dagger = \sqrt{s_-(A) s_-(C)} = 0.954$ and the s value of the s_- (B) case. The $s_+^\dagger$ is also consistent with $s^\dagger = \sqrt{s_+(A) s_+(B)} = 1.049$. The predicted q is similar to empirical q values of the s_- cases by a factor of $\sim$2.

For the s_- case, we find several degenerate solutions within $\Delta\chi^2 < 1.0$. These solutions show three categories of geometries as shown in Figure 5. The A, B, and C families are produced by the different source trajectories, which travel over the inner, intermediate, and outer parts of the caustics,

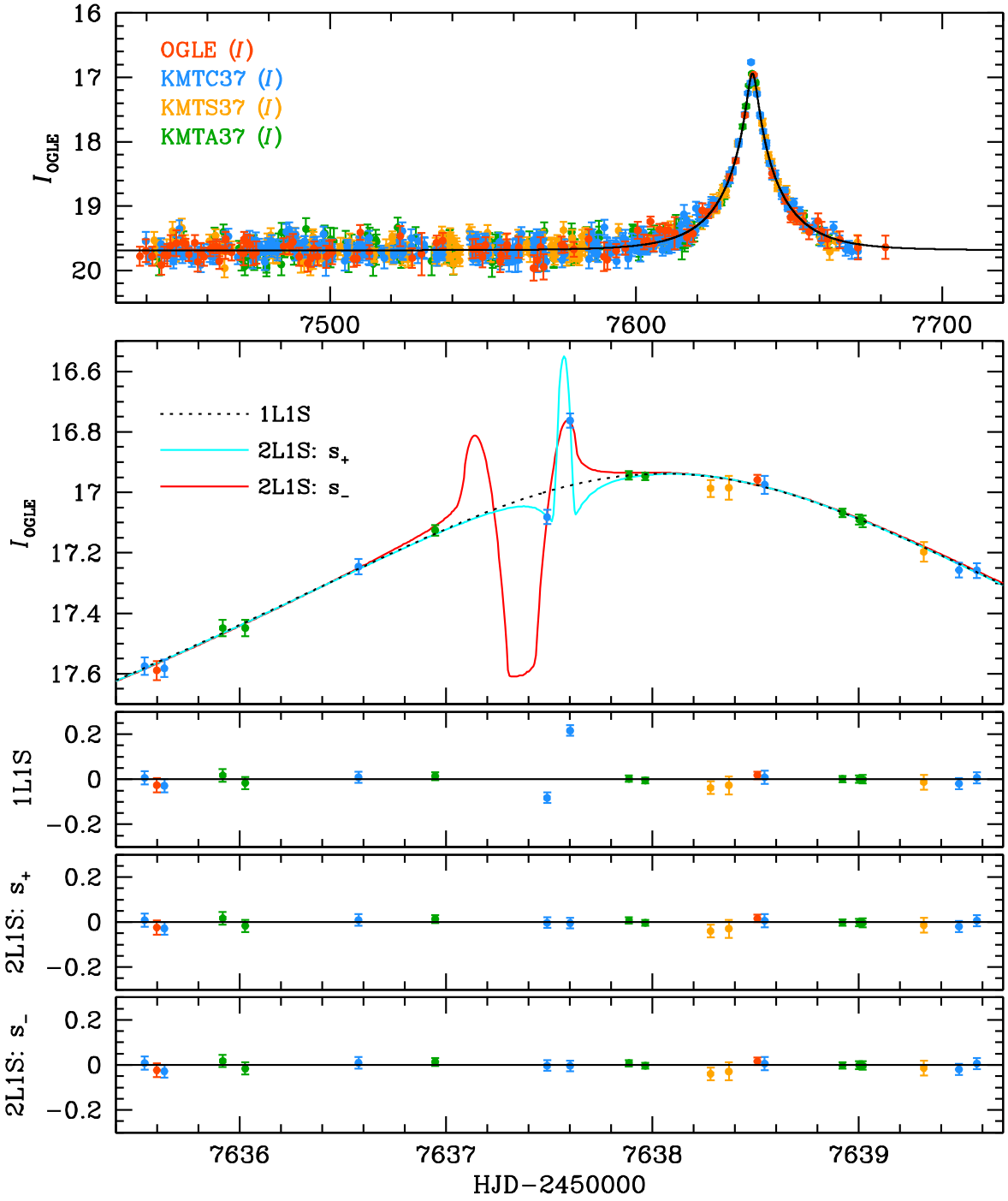

Figure 4. Light curve of MOA-2016-BLG-526 with 2L1S solutions compared to the 1L1S models.

respectively. Indeed, this kind of degeneracy was introduced in the analysis of OGLE-2017-BLG-0173Lb (Hwang et al. 2018). Thus, we adopt the $\Delta\xi$ ($\equiv u_0 \csc\alpha - [s - s^{-1}]$) parameter described in Hwang et al. (2018) to separate and extract each family (see dotted lines in the upper left panel of Figure 5). We present the best-fit solution for each family as a representative. For the s_+ case, we find two solutions caused by the inner/outer degeneracy, which cannot be distinguished (i.e., $\Delta\chi^2 = 0.2$). In Figure 6, we present the light curves of s_+ solutions with their geometries. For consistency, we also present $\Delta\xi - \log_{10}(q)$ space to show the locations of each solution, which are clearly divided into two categories. Although there exist several degenerate solutions with $\Delta\chi^2 \lesssim 1.0$, all solutions have mass ratios less than 0.03. Thus, we conclude that this event was caused by a planetary lens system.

Because of the relatively long timescale ($t_{\rm E} \sim 20$ days) for all solutions, we test the APRX effect for this event. However, we find a negligible χ^2 improvement of $\Delta\chi^2 = 1.55$ compared to the best fit of STD solution and no meaningful constraints on $\boldsymbol{\pi_E}$. Thus, we treat the STD models as our fiducial solutions. Note that, because of the sparse coverage, we cannot measure the ρ_* for all STD cases even though some cases show caustic-crossing features.

Table 5
The Parameters of Degenerate 2L1S Solutions for MOA-2016-BLG-526

Parameter	s_- (A)	s_- (B)	s_- (C)	s_+ (A)	s_+ (B)
$\chi^2/N_{\rm data}$	2218.429/2220	2218.431/2220	2218.648/2220	2219.283/2220	2219.463/2220
$\Delta\chi^2$	⋯ (best fit)	0.002	0.219	0.854	1.034
t_0 [HJD′]	7638.076 ± 0.021	7638.075 ± 0.021	7638.078 ± 0.022	7638.056 ± 0.019	7638.059 ± 0.019
u_0	0.086 ± 0.005	0.087 ± 0.005	0.090 ± 0.005	0.085 ± 0.005	0.086 ± 0.005
$t_{\rm E}$ [days]	19.483 ± 0.771	19.446 ± 0.758	19.037 ± 0.774	19.558 ± 0.752	19.348 ± 0.754
s	0.944 ± 0.005	0.954 ± 0.003	0.965 ± 0.006	1.062 ± 0.013	1.036 ± 0.014
q ($\times 10^{-4}$)	1.760 ± 0.467	1.184 ± 0.329	1.593 ± 0.524	0.605 ± 0.620	0.475 ± 0.751
$\langle \log_{10} q \rangle$	-3.772 ± 0.119	-3.957 ± 0.128	-3.787 ± 0.138	-4.096 ± 0.229	-4.081 ± 0.239
α [rad]	5.109 ± 0.016	5.104 ± 0.016	5.103 ± 0.017	1.855 ± 0.018	1.855 ± 0.018
$\rho_{*,\rm limit}$	<0.007	<0.009	<0.009	<0.007	<0.007

Note. HJD′ = HJD−2,450,000.0. We note that the ρ_* is not measured for any 2L1S case. We present 3σ upper limits on the ρ_* values (i.e., $\rho_{*,\rm limit}$).

Lastly, the s_+ solutions exhibit a bump-like anomaly, which can yield a 2L1S/1L2S degeneracy. Thus we check whether or not the 1L2S model can explain the anomaly. We find that the 1L2S model cannot explain the KMTC point at HJD′ = 7637.4903, which shows a shallow dip relative to the 1L1S fits. Also, we find that the 1L2S interpretation is fine-tuned to describe the KMTC point at HJD′ = 7637.6021. That is, to fit this point, the 1L2S model has $q_{\rm flux} \sim \mathcal{O}(10^{-4})$, which is nonphysical. Thus, we conclude that there is no 2L1S/1L2S degeneracy for this event despite the fact that, due to the lack of covered data points, $\Delta\chi^2 = 11.7$ between the 2L1S and 1L2S models, which is smaller than our formal threshold.

We consider MOA-2016-BLG-526 to be a clear planet detection because all classes of solutions are planetary, and the anomalous points are real. However, this planet also illustrates that the utility of a criterion requiring at least three data points contributes to the signal for planets that are part of statistical samples (e.g., as in Shvartzvald et al. 2016). In this case, the fact that there are multiple solutions is a product of there only being two points on the anomaly with the result that there is substantial uncertainty in, e.g., the mass ratio of the planet. As seen in Figure 4, a third observation at almost any point during the anomaly could have differentiated between the families of the solution. In conclusion, whether or not this particular planet should be included in a given statistical sample must be carefully evaluated based on the criteria for defining that sample, and, conversely, this event serves as a good edge case to consider when defining such criteria.

Ultimately, whether or not this particular planet is included in a given statistical sample will depend on what criteria are chosen to define that sample (such as the minimum number of data points in an anomaly), but it is outside of the scope of this work to define exactly what those criteria should be.

3.2.4. KMT-2016-BLG-2321

As shown in Figure 7, the light curve of KMT-2016-BLG-2321 exhibits an apparent anomaly at HJD′ ∼ 7621.5 that has a short duration (∼0.35 days). We find that the anomaly can be explained by 2L1S models with caustic-crossing geometries. In Table 6, we present the best-fit parameters of the 2L1S solutions. Indeed, we predict $s_-^\dagger = 0.912$, and $s_+^\dagger = 1.097$ from the heuristic analysis ($\tau_{\rm anom} = -0.0737$, $t_{\rm anom} = 0.1853$). The predicted $s_+^\dagger$ value corresponds with the empirical value of $s^\dagger = \sqrt{s_{\rm outer} s_{\rm inner}} = 1.096$. Although the 2L1S solutions caused by the inner/outer degeneracy cannot be distinguished ($\Delta\chi^2 = 0.66$), the mass ratios of both solutions indicate that the event was caused by a planetary lens system, i.e., $q \sim \mathcal{O}(10^{-3})$.

Because of the long timescales (∼57 days) for both solutions, we test the APRX effect. However, we find no χ^2 improvement (the STD best-fit solution shows better fits than the APRX model by $\Delta\chi^2 = 0.33$). Even though we additionally include the OBT effect (i.e., APRX+OBT model), we find a negligible χ^2 improvement of $\Delta\chi^2 = 1.28$ and no meaningful constraints on $\boldsymbol{\pi_E}$. Thus, we conclude that the higher-order effects are not available for this event. We note that, despite caustic-crossing features, the ρ_* measurements are uncertain because the data coverage is not optimal.

Because of the caustic-crossing feature, we expect the 2L1S/1L2S degeneracy will not be an obstacle to claim planet detection. However, because the coverage is not optimal, we check the 1L2S model for confirmation. As expected, we find the 1L2S model is disfavored by $\Delta\chi^2 = 132.56$, which cannot explain the caustic-crossing feature despite the nonoptimal coverage.

3.3. Planet Candidates

We find seven planet candidates among the 11 events, which are analyzed using the TLC data sets. These events have the possibility to be caused by a planetary lens system. However, these candidates cannot satisfy all our criteria to firmly claim planet detection. For example, there exist competing binary-lens solutions that cannot be resolved, or there is the 2L1S/1L2S degeneracy to prevent claiming the planet detection. Although we cannot firmly claim planet detection, there still remains the possibility that these events might be caused by a planetary system unless we have clear evidence against this conclusion. Hence, we report these planet candidates with the details of the light-curve analyses for the record, in case there is an opportunity to conclusively reveal their nature in the future.

3.3.1. KMT-2016-BLG-1243

The light curve of KMT-2016-BLG-1243 exhibits a flat-topped deviation at the peak as shown in Figure 8. Such an anomaly may be caused solely by finite-source (FS) effects or by the combination of FS effects and the central caustic of a 2L1S model. In Table 7, we present the model parameters of these various competing models. When fitting for a 1L1S+FS model, we find $\chi^2 = 685.63$.

Fitting for 2L1S models, (i.e., $s \pm$ cases), we find solutions that fit better than the 1L1S+FS model by $\Delta\chi^2 = 9.6$. These solutions imply that the lens system consists of binary stars (see

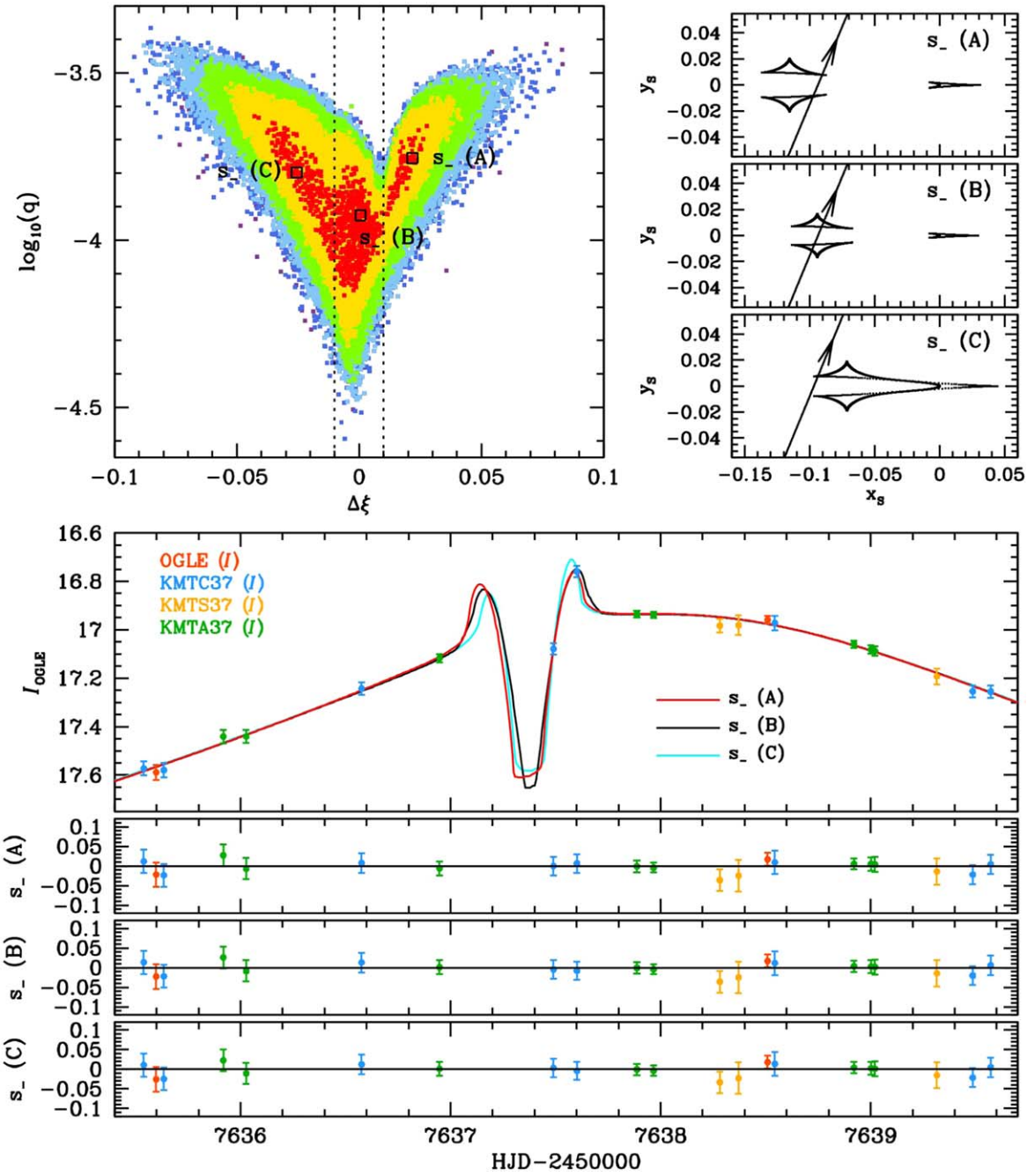

Figure 5. Light curve of MOA-2016-BLG-526 with the family of degenerate 2L1S s_- models with the $\Delta\xi-\log_{10}(q)$ space. In the $\Delta\xi-\log_{10}(q)$ space (upper left panel), each color represents $\Delta\chi^2 \leqslant n^2$ from the best-fit χ^2 where $n = 1$ (red), 2 (yellow), 3 (green), 4 (light blue), 5 (blue), and 6 (purple), respectively.

Table 7). However, we also find that there exist competing 2L1S models ($\Delta\chi^2 < 4.8$) that indicate that the lens is likely to be a planetary system (i.e., $q < 0.03$). Indeed, we predict $s_-^\dagger = 0.990$, and $s_+^\dagger = 1.011$ from the heuristic analysis ($\tau_{\rm anom} = 0.0067$, $u_{\rm anom} = 0.0211$), which is similar to the $s^\dagger \equiv \sqrt{s_- s_+} = 1.024$ for the combination of P3 and P4 cases. In Figure 9, we present the residuals of the anomaly part for all degenerate models with their caustic geometries. By comparing them, we find the χ^2 difference mostly comes from fits between HJD′ = 7643.5 ∼ 7646.0. However, because of the sparse coverage, the $\Delta\chi^2$ of all degenerate cases is smaller than our χ^2 criterion ($\Delta\chi^2 = 10.0$) to claim a planet detection. In particular, the best-fit model of the planet case shows only $\Delta\chi^2 = 1.8$.

Lastly, we note that we test the APRX effect because of the long timescales (i.e., $t_{\rm E} > 70$ days). However, we find negligible χ^2 improvement of 2.8 compared to the STD best-fit case.

However, in addition to the χ^2 criterion, we can also apply a Galactic prior to these solutions. In the case of the planetary models, the model parameters imply that $\mu_{\rm rel} = \theta_*/(\rho_* t_{\rm E}) \sim 0.08$ mas yr^{-1} by assuming a dwarf source (i.e., $\theta_* \sim 0.5\,\mu$as). From the argument following Equation (22) of Gould (2022), the probability of such an exceptionally small $\mu_{\rm rel}$ is $(\mu_{\rm rel}/6\ {\rm mas\ yr^{-1}})^2 \sim 1.8 \times 10^{-4}$. Likewise, the 1L1S+FS model is equally unlikely that it has similar parameters. Hence, although this event is technically a planet candidate based on $\Delta\chi^2$, those solutions are extremely unlikely to be the true solution after taking physical considerations into account.

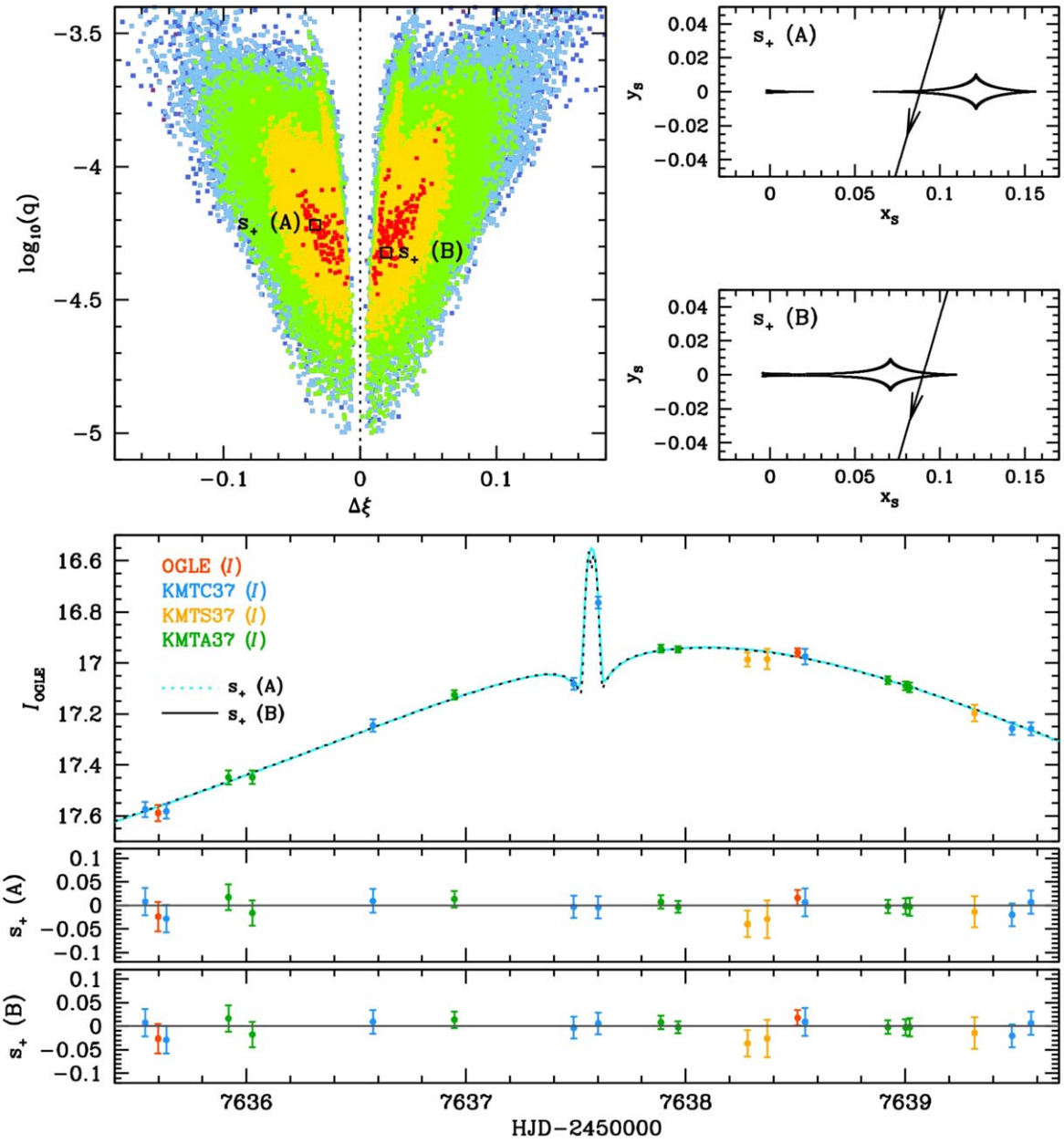

Figure 6. Light curve of MOA-2016-BLG-526 with the degenerate 2L1S s_+ models and the $\Delta\xi-\log_{10}(q)$ space. The color scheme of the $\Delta\xi-\log_{10}(q)$ space is identical to that of Figure 5.

3.3.2. OGLE-2016-BLG-0336

As shown in Figure 10, the light curve of OGLE-2016-BLG-0336 (which we identified as KMT-2016-BLG-1406) shows an apparent bump-shaped anomaly at the peak (HJD′ = 7481.7), which was covered by KMTC and KMTS observations. We find that the anomaly can be explained by several models presented in Table 8. Similar to the case of MOA-2016-BLG-526, there exist three 2L1S solutions caused by different caustic geometries (i.e., (A) caustic-crossing, (B) inner, and (C) outer trajectories). These cases cannot be resolved (i.e., $\Delta\chi^2 \lesssim 1$). Indeed, we predict $s_-^\dagger = 0.919$, and $s_+^\dagger = 1.088$ from the heuristic analysis ($\tau_{\rm anom} = 0.0280$, $u_{\rm anom} = 0.1684$). The $s_+^\dagger$ is well consistent with the best fit of $s_+ = 1.089$. We present the $\Delta\xi-\log_{10}(q)$ space to show the locations of these degenerate cases (see the right upper panel in Figure 10). Although we cannot resolve the degeneracy, the mass ratios of all 2L1S solutions imply that the lens is likely to be a planetary lens system (i.e., $q < 0.03$).

However, the bump-shaped anomaly is a typical type to have the 2L1S/1L2S degeneracy. We find that the 1L2S model can describe the anomaly well. Moreover, the $\Delta\chi^2$ compared to the 2L1S best-fit model is only 1.13. Because there are only weak constraints on $\rho_{*,\rm S1}$ and $\rho_{*,\rm S2}$, and a relatively large separation between the two sources ($\Delta u \sim 0.17$), we cannot place any additional meaningful constraints from physical considerations. Based on currently available data sets and analysis results, we cannot resolve the 2L1S/1L2S degeneracy for this event. Thus, we treat this event as a planet candidate unless we have additional evidence to rule out the 1L2S solution.

Note that we have checked the APRX effect for this event because of the relatively long timescale ($t_{\rm E} \sim 25$ days). We find the χ^2 improvement of 14.83 for the APRX-included model.

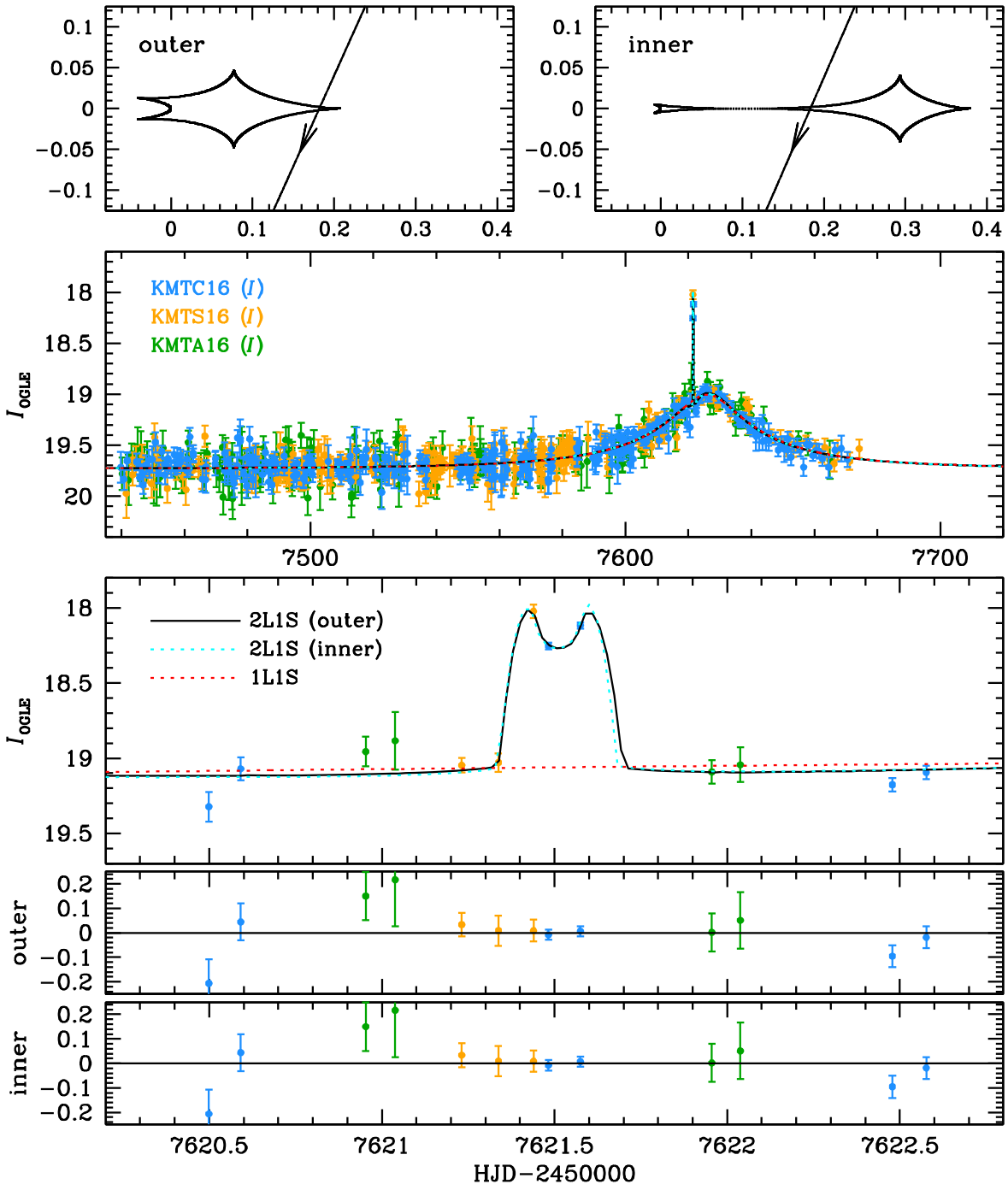

Figure 7. Light curve of KMT-2016-BLG-2321 with the 2L1S solutions compared to the 1L1S models.

However, we find that the χ^2 improvements between data sets are inconsistent. Indeed, the STD model shows better fits for the KMTC data that yields $\Delta\chi^2 \sim 10.0$. In contrast, for the other data (OGLE, MOA, and KMTA), the APRX model shows better fits that yield $\Delta\chi^2 \sim 8.0$, 12.0, and 4.0, respectively. For KMTS, there is no χ^2 improvement. This inconsistency makes us suspect the APRX detection is unreliable, similar to the case of OGLE-2016-BLG-1598. Also, these improvements only come from the baseline, which can have systematics. Thus, we conclude that the APRX measurement is not robust. The STD models should be the fiducial solutions for this event.

3.3.3. OGLE-2016-BLG-0882

The light curve of OGLE-2016-BLG-0882 (which we identified as KMT-2016-BLG-1449) shows anomalies at the peak, which have complex features consisting of three bump-shaped anomalies as shown in Figure 11. We find no 2L1S models that can correctly describe the anomalies. Thus, we try to describe the anomalies using 2L2S and 3L1S interpretations. We find the best-fit 2L2S model can describe all anomalies, which implies that the lens system consists of binary stars (i.e., $q \sim 0.3$). However, we also find that there exist competing solutions having $\Delta\chi^2 < 10.0$. In Table 9, we present these degenerate 2L2S solutions. Among them, one case satisfies our

Table 6
The Parameters of Degenerate 2L1S Solutions for KMT-2016-BLG-2321

Parameter	Outer	Inner
$\chi^2/N_{\rm data}$	882.415/883	883.079/883
$\Delta\chi^2$	⋯ (best fit)	0.664
t_0 [HJD′]	7625.748 ± 0.210	7625.684 ± 0.216
u_0	0.166 ± 0.018	0.168 ± 0.020
$t_{\rm E}$ [days]	56.847 ± 4.562	56.966 ± 6.387
s	1.039 ± 0.014	1.157 ± 0.012
q ($\times 10^{-4}$)	12.326 ± 2.992	12.703 ± 3.200
$\langle \log_{10} q \rangle$	-2.967 ± 0.115	-2.948 ± 0.118
α [rad]	1.993 ± 0.020	1.981 ± 0.021
$\rho_{*,\rm limit}$ ($\times 10^{-3}$)	<1.466	<1.268

Note. HJD′ = HJD−2,450,000.0. We note that ρ_* is not measured for any case. We present 3σ upper limits on the ρ_* values (i.e., $\rho_{*,\rm limit}$).

mass ratio criterion for planet detection (i.e., $q \sim 0.01 < 0.03$). The $\Delta\chi^2$ between binary and planetary solutions is only 5.8, which is not enough to distinguish them.

In addition, because the complex anomaly could be described by the 3L1S interpretation, we try to find a possible planetary solution. We find a plausible 3L1S model that can describe the anomalies (see Figure 11 and Table 9). This 3L1S model implies that the third body is likely to be a planet (i.e., $q_2 \sim 0.011$). However, this 3L1S model shows $\Delta\chi^2 > 32.0$ compared to the best-fit 2L2S models. If we consider the satisfied 2L2S models, the 3L1S has worse fits by $\Delta\chi^2 > 23.0$. Thus, the 3L1S case can be nominally ruled out considering our χ^2 criterion. However, we do not ignore the possibility of the 3L1S solution because of two reasons. First, our search for 3L1S models was not exhaustive because of the technical difficulty of conducting a full search of the six parameters required to describe the two companions and source trajectory angle (i.e., s_1, q_1, s_2, q_2, ψ, and α), which are most sensitive to explaining the anomaly. Thus, there may exist alternative 3L1S solution(s) having better χ^2. Second, for this event, the data sets have systematics on the anomaly part that are not explained by any model. Hence, our χ^2 criteria may not be sufficient in this case. Thus, we present the 3L1S planetary solution as one alternative possibility of planetary systems that could produce the anomaly. Indeed, if we rule out this 3L1S case, there still remains the binary/planet degeneracy in the 2L2S solutions. Thus, we treat this event as a planet candidate including the possible 3L1S solution.

Lastly, we note that we test the APRX effect because the models show that the timescales are longer than 32 days. However, we find only negligible χ^2 improvement (i.e., $\Delta\chi^2 \sim 4.7$) when the APRX effect is considered. Thus, we conclude the STD models are fiducial solutions for this event.

3.3.4. OGLE-2016-BLG-1704

The light curve of OGLE-2016-BLG-1704 (which we identified as KMT-2016-BLG-1609) shows apparent deviations from the 1L1S fit. The anomaly can be explained by various models. In Figure 12, we present these models with their caustic geometries. As shown in Table 10, the best-fit model (see the (A) case) implies that the lens system consists of binary stars (i.e., $q \sim 0.53$). However, there exist degenerate models having $\Delta\chi^2 < 10.0$. The mass ratio of the (B) case nominally indicates that the lens is likely to be a binary star system. However, this model is caused by the Chang & Refsdal lensing (Chang & Refsdal 1979), which has large uncertainties in the (s, q) parameters. Hence, the mass ratio satisfies our mass ratio criterion (i.e., $q < 0.03$) within 1σ. For the (C) case, the mass ratio indicates the lens system could have a planet. The (D) solution can be nominally resolved by $\Delta\chi^2 = 13.1$, which is slightly larger than our χ^2 criterion. However, by considering the systematics in the data sets, we cannot firmly rule out this case. Thus, we present this planet-like case for completeness. For the (C) and (D) cases, the heuristic analysis ($\tau_{\rm anom} = 0.0217$, $u_{\rm anom} = 0.0752$) predicts $s_-^\dagger = 0.963$, and $s_+^\dagger = 1.038$, which is similar to the empirical value of $s^\dagger = \sqrt{s_{-,(C)} s_{+,(D)}} = 1.035$.

Lastly, we find that a 1L2S model can also explain the anomaly. The $\Delta\chi^2$ between the best-fit and 1L2S models is only 3.4, which cannot be resolved. Thus, we treat this event as a planet candidate because of the binary/planet and 2L1S/1L2S degeneracies.

We note that we have tested the APRX effect because of the relatively long timescales (i.e., $t_{\rm E} > 32$ days). We find the negligible χ^2 improvement of 5.0 when the APRX effect is included. Thus, we conclude that the STD models are the fiducial solutions for this event.

3.3.5. OGLE-2016-BLG-1408

OGLE-2016-BLG-1408 (which we identified as KMT-2016-BLG-1630) is a long timescale event that has an anomaly at the peak on the light curve. In Figure 13, we present the light curve with the 2L1S and 1L1S models of the STD and APRX cases. Because of the long timescale (i.e., $t_{\rm E} > 96$ days), we find that the APRX effect is essential to describe the observed light curve. In particular, as shown in Figure 13, it is impossible to describe the 2017 data without the APRX effect. Also, the 2L1S models with the APRX effect are the only interpretations that can explain the anomaly at the peak.

However, we find that several 2L1S APRX models can describe the whole light curve, which cannot be distinguished from each other. In Figure 14, we present these degenerate solutions with their caustic geometries. We also present model parameters for the cases in Table 11. The best-fit case indicates that the lens could be a planetary system (i.e., $q \sim \mathcal{O}(10^{-3})$). There exist five competing planetary cases caused by the close/wide (Griest & Safizadeh 1998) and ecliptic (Smith et al. 2003; Jiang et al. 2004; Poindexter et al. 2005) degeneracies. Although, among the planetary cases, the wide $u_0 \pm$ cases can be nominally resolved by $\Delta\chi^2 > 10.0$, we present them for completeness and comparison to the binary-lens cases.

Despite the best-fit model implying that the lens has a planet, we find that there also exist competing binary-lens cases having $\Delta\chi^2 \lesssim 5.4$. In particular, the best fit of the binary case shows only $\Delta\chi^2 = 0.9$.

We note that we conduct tests for the APRX effect because the effect is essential to finding the solutions. First, we have tested the OBT effect, which can affect the APRX measurement. We find no χ^2 improvement when the OBT effect is considered (i.e., $\Delta\chi^2\,[\rm OBT - APRX] = 0.3$). Moreover, we find that the OBT effect does not affect the uncertainties of the APRX measurement. Second, we have tested whether the xallarap effect can mimic the APRX effect. Similar to the OBT case, we find that the xallarap effect does not improve the fits (i.e., $\Delta\chi^2\,[\rm xallarap - APRX] = 0.4$). Also, as shown in Figure 15, the best-fit xallarap model has $P = 1$ yr, which is consistent with the orbital period of the Earth. Both facts imply

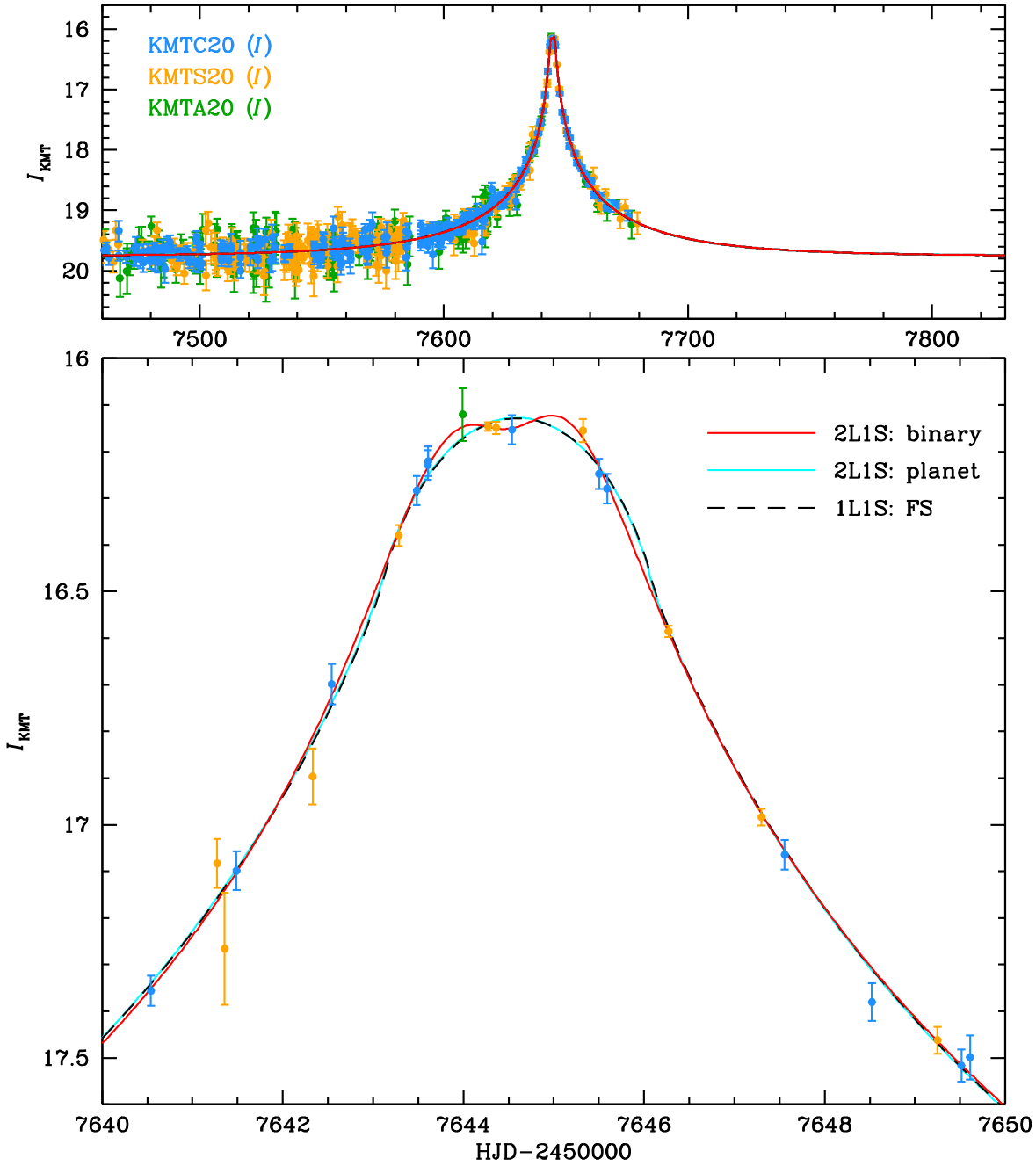

Figure 8. Light curve of KMT-2016-BLG-1243 with 2L1S binary and planet models compared to the 1L1S model. The 1L1S model includes the finite-source effect (FS).

that the effect on the light curve is caused by APRX rather than xallarap. Hence, we conclude that the APRX models are the fiducial solutions for this event. We also note that we can measure ρ_* for only the resonant ($u_0 \pm$) cases induced by the caustic-crossing geometries. For other cases, we cannot robustly measure the ρ_* because of the non-caustic-crossing geometries.

Lastly, we check the 2L1S/1L2S degeneracy because the bump-like anomaly can be explained by the 1L2S interpretation. We find that the 1L2S model with the APRX effect shows better fits by $\Delta\chi^2 = 6.7$ compared to the best fit of the 2L1S APRX models. Thus, this 1L2S model can be an alternative solution for this event. At this moment, we cannot resolve both planet/binary and 2L1S/1L2S degeneracies for this event because of insufficient $\Delta\chi^2$. Hence, we treat OGLE-2016-BLG-1408 as a planet candidate.

3.3.6. KMT-2016-BLG-2399

The light curve of KMT-2016-BLG-2399 shows a bump-shaped anomaly on the rising part (HJD′ $\sim$ 7626). As shown in Figure 16, the anomaly can be described by a binary-lens model that contains a low-mass object (i.e., $q \sim 0.057$). We also find that planet-like models can plausibly describe the anomaly. In Table 12, we present the model parameters of possible solutions for this event. Indeed, the heuristic analysis ($\tau_{\rm anom} = -0.2813$, $u_{\rm anom} = 0.2924$) predicts $s_-^\dagger = 0.864$, and $s_+^\dagger = 1.157$, which is consistent with $s^\dagger \equiv \sqrt{s_+(A)s_-(C)} = 0.864$. In addition, we

Table 7
The Parameters of Degenerate Solutions for KMT-2016-BLG-1243

Case	2L1S: Binary		2L1S: Planet				1L1S	
Parameter	B1	B2	P1	P2	P3	P4	Parameter	FS
$\chi^2/N_{\rm data}$	676.060/677	676.254/677	677.904/677	680.261/677	680.065/677	680.823/677	$\chi^2/N_{\rm data}$	685.628/677
$\Delta\chi^2$	⋯ (best fit)	0.194	1.844	4.201	4.005	4.763	$\Delta\chi^2$	9.568
t_0 [HJD′]	7644.621 ± 0.022	7644.596 ± 0.020	7644.588 ± 0.019	7644.587 ± 0.019	7644.583 ± 0.019	7644.598 ± 0.019	t_0 [HJD′]	7644.599 ± 0.018
u_0	0.018 ± 0.001	0.015 ± 0.001	0.023 ± 0.002	0.022 ± 0.002	0.024 ± 0.002	0.024 ± 0.002	u_0	0.023 ± 0.002
$t_{\rm E}$ [days]	74.153 ± 4.402	85.562 ± 5.320	72.871 ± 4.421	77.779 ± 4.802	70.841 ± 4.591	71.117 ± 4.656	$t_{\rm E}$ [days]	74.794 ± 4.593
s	0.162 ± 0.023	8.260 ± 1.095	$1.167^{+0.584}_{-1.002}$	$0.407^{+2.387}_{-0.248}$	$2.945^{+2.006}_{-2.812}$	$0.356^{+4.462}_{-0.223}$	⋯	⋯
q	0.200 ± 0.138	0.336 ± 0.104	$(0.759^{+45.951}_{-0.759}) \times 10^{-4}$	$0.008^{+0.004}_{-0.008}$	$0.027^{+0.024}_{-0.027}$	$0.025^{+0.022}_{-0.025}$	⋯	⋯
$\langle \log_{10} q \rangle$	-0.632 ± 0.184	-0.559 ± 0.157	-3.359 ± 0.955	-3.358 ± 1.013	-3.311 ± 1.014	-3.333 ± 0.983	⋯	⋯
α [rad]	4.043 ± 0.057	4.016 ± 0.053	-6.219 ± 3.490	6.058 ± 3.137	3.811 ± 3.638	-2.417 ± 3.479	⋯	⋯
ρ_*	<0.016	<0.014	0.031 ± 0.002	0.029 ± 0.002	0.032 ± 0.002	0.032 ± 0.002	ρ_*	0.030 ± 0.002

Note. HJD′ = HJD−2,450,000.0. For the ρ_* parameter, the inequality sign indicates the upper limit on ρ_* (i.e., 3σ), because we cannot robustly measure ρ_* for those cases.

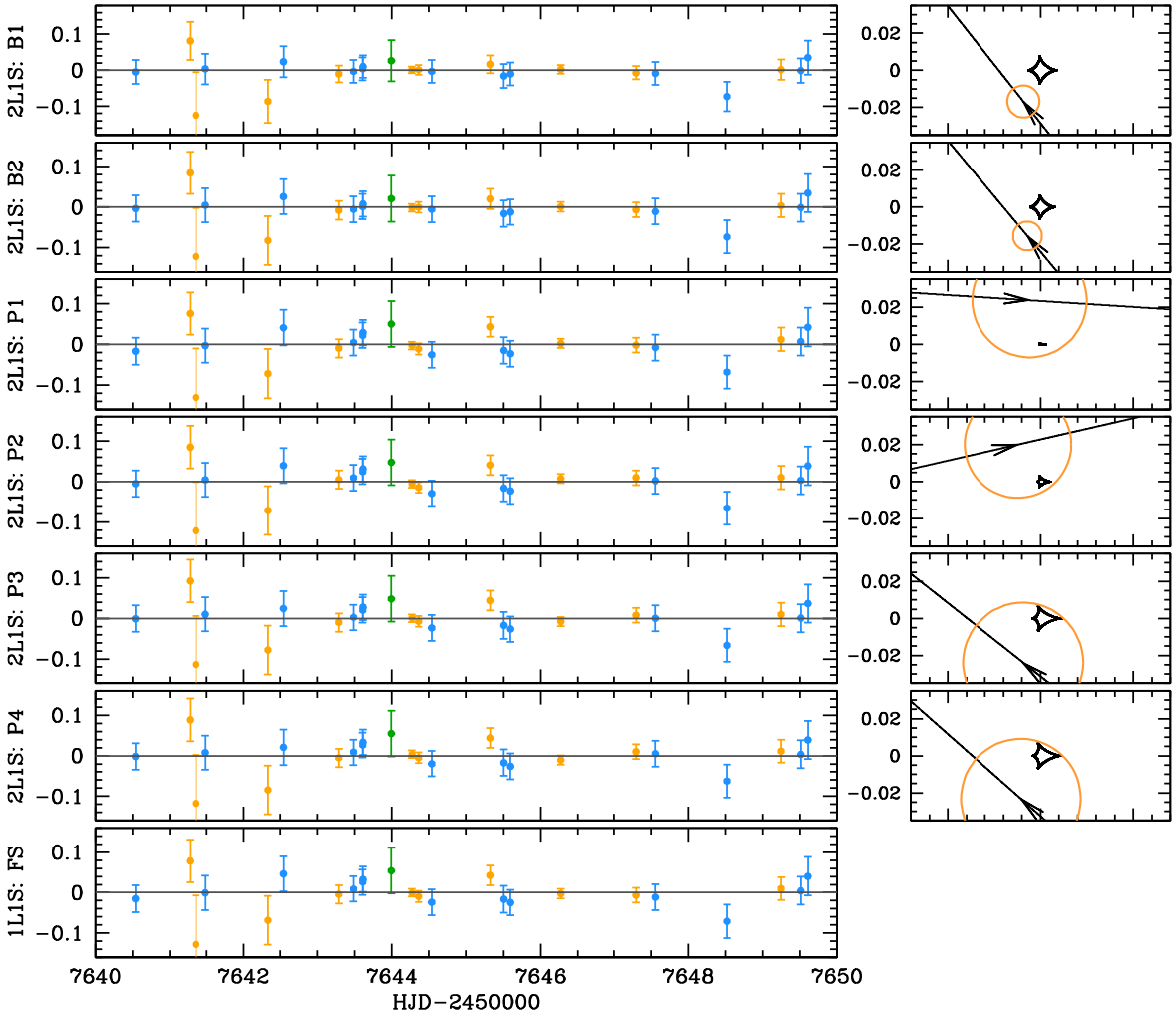

Figure 9. OGLE-2016-BLG-1258: Residuals of each case shown in Table 7 with its caustic geometry. We show the residuals for the zoom-in part of Figure 8.

find that the bump-shaped anomaly can also be plausibly described by a 1L2S model, which shows $\Delta\chi^2 = 14.2$ compared to the best-fit model.

We note that the planet-like cases are borderline given our criteria. First, for the B case, the mass ratio is ∼0.030, which is consistent with the q criterion, while the C case does not satisfy the q criterion. However, the C model shows a very short timescale (i.e., $t_{\rm E} \sim 8$ days) with a relatively small q value (i.e., $q \sim 0.049$), which implies the component of the lens system would be a planet. Second, both cases are nominally resolved by the χ^2 criterion (i.e., $\Delta\chi^2 = 10.0$). However, the B case ($\Delta\chi^2 = 10.2$) is very close to our χ^2 criterion. By considering the systematics in the data, we cannot firmly rule out the model based on current data. We note that the B model exhibits a sharp bump at HJD′ ∼ 7620. However, there are no available data points observed by either KMTNet or OGLE.

Even if we can rule out the C and 1L2S cases by simply adopting our criteria, there still remains a possible planet case (i.e., the B case) that cannot be clearly ruled out. Thus, we treat this event as a planet candidate.

Note that we have tested the APRX effect for this event because the best-fit solution has a sufficiently long timescale (i.e., $t_{\rm E} \sim 19$ days) that the APRX effect may be detected. However, we find a negligible χ^2 improvement of 0.9 when we consider the APRX effect. Thus, the STD cases are the fiducial models for this event. Finally, we note that we can measure the ρ_* values for the A (caustic-crossing) and C (buried caustic) cases (see caustic geometries in Figure 16).

3.3.7. KMT-2016-BLG-2473

The light curve of KMT-2016-BLG-2473 exhibits anomalies from the 1L1S model ($\Delta\chi^2 = 171.0$) during HJD′ = 7500 ∼ 7520, as shown in Figure 17. The anomalies can be explained by a 2L1S model (note that the heuristic analysis is not valid for this event). The mass ratio of this best-fit model indicates that the lens system is likely to be a planetary system (i.e., $q \sim 0.011$). However, we find that a 1L2S model is also able to plausibly describe the anomaly. In Table 13, we present the model parameters of the 2L1S and 1L2S models.

The 2L1S and 1L2S models themselves show a clear difference at HJD′ ∼ 7505.0, which seems to be a shallow bump-shaped anomaly. However, the $\Delta\chi^2$ between them is only 10.3, which does not satisfy our criterion to resolve the 2L1S/1L2S degeneracy. The small $\Delta\chi^2$ is caused by severe systematics in data sets because the event experienced heavy extinction (i.e., $A_I \sim 4.9$). Thus, we treat this event as a planet candidate because we do not have any conclusive evidence to resolve the 2L1S/1L2S degeneracy.

Note that we have tested the APRX effect because of the long timescale (i.e., $t_{\rm E} \sim 47$ days). We find a small χ^2

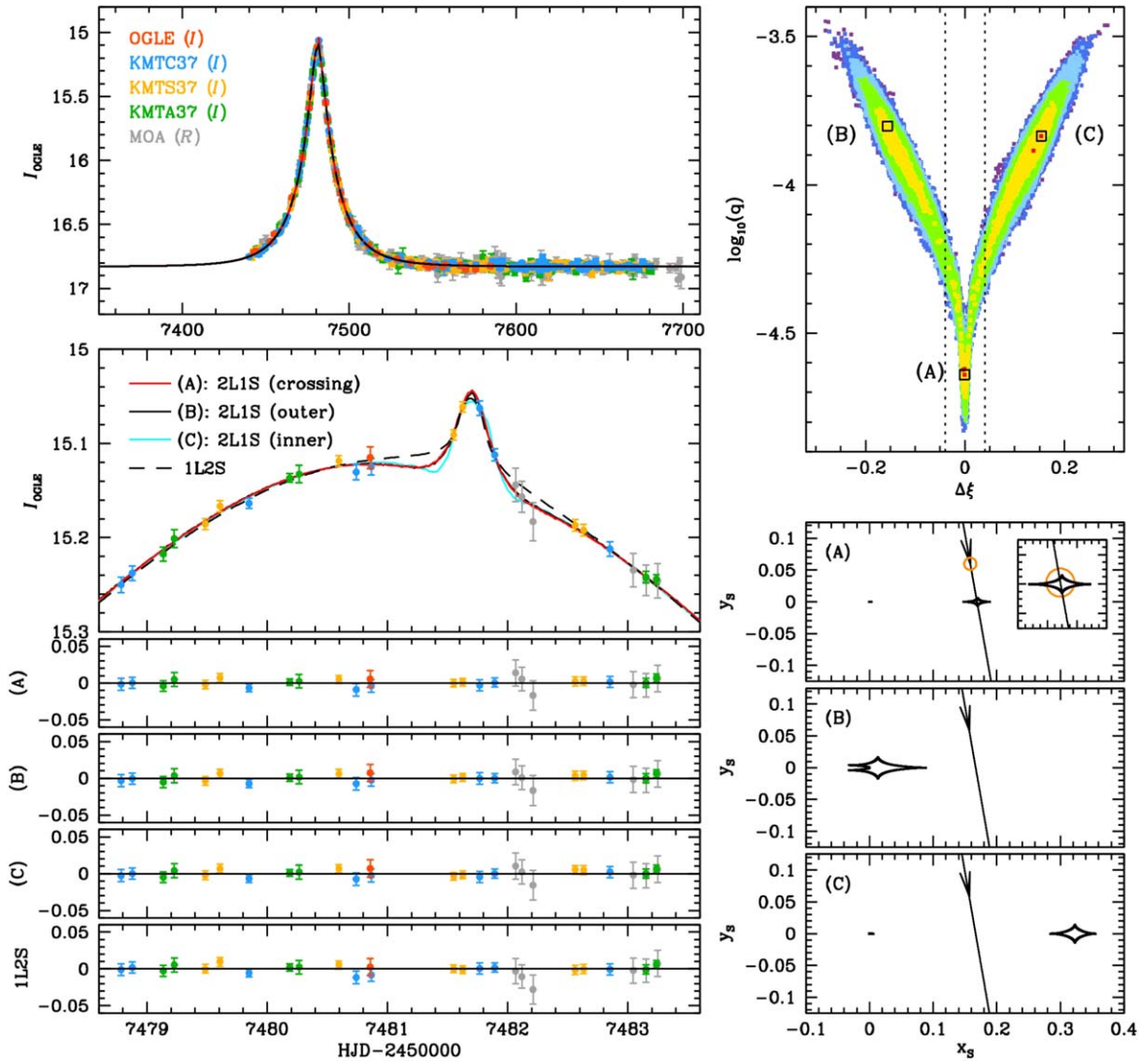

Figure 10. Light curves of OGLE-2016-BLG-0336 with degenerate models and their residuals. We present $\Delta\xi - \log_{10}(q)$ space to show the local minima for the 2L1S models. We also present their caustic geometries.

Table 8
The Parameters of Degenerate Solutions for OGLE-2016-BLG-0336

Parameter	A: 2L1S	B: 2L1S	C: 2L1S	Parameter	1L2S
$\chi^2/N_{\rm data}$	7847.419/7875	7848.177/7875	7848.525/7875	$\chi^2/N_{\rm data}$	7848.545/7875
$\Delta\chi^2$	⋯ (best fit)	0.758	1.106	$\Delta\chi^2$	1.126
t_0 [HJD′]	7480.996 ± 0.009	7481.006 ± 0.009	7481.009 ± 0.009	$t_{0,\rm S1}$ [HJD′]	7480.995 ± 0.010
u_0	0.166 ± 0.002	0.164 ± 0.002	0.164 ± 0.002	$u_{0,\rm S1}$	0.168 ± 0.006
$t_{\rm E}$ [days]	24.513 ± 0.227	24.621 ± 0.230	24.623 ± 0.230	$t_{\rm E}$ [days]	24.495 ± 0.246
s	1.089 ± 0.003	1.007 ± 0.016	1.174 ± 0.019	$t_{0,\rm S2}$ [HJD′]	7481.700 ± 0.012
q ($\times 10^{-4}$)	0.229 ± 0.032	1.462 ± 0.319	1.577 ± 0.340	$u_{0,\rm S2}$	−0.004 ± 0.003
$\langle \log_{10} q \rangle$	−4.619 ± 0.059	−3.835 ± 0.110	−3.802 ± 0.115	$q_{\rm flux}$	0.002 ± 0.001
α [rad]	1.396 ± 0.003	1.399 ± 0.004	1.400 ± 0.004	$\rho_{*,\rm S1}$	<0.190
ρ_*	0.010 ± 0.001	<0.011	<0.011	$\rho_{*,\rm S2}$	<0.009

Note. HJD′ = HJD−2,450,000.0. For the ρ_* parameter, the inequality sign indicates the upper limit on ρ_* (i.e., 3σ), because we cannot robustly measure ρ_* for those cases.

improvement of 5.8 when we consider the APRX effect. However, the improvement comes from the baseline, which has severe systematics. Thus, we conclude that the APRX effect is not robust. Hence, the STD models are the fiducial solutions for this event. Lastly, we note that the ρ_* can be measured for the 2L1S case from the caustic-crossing feature.

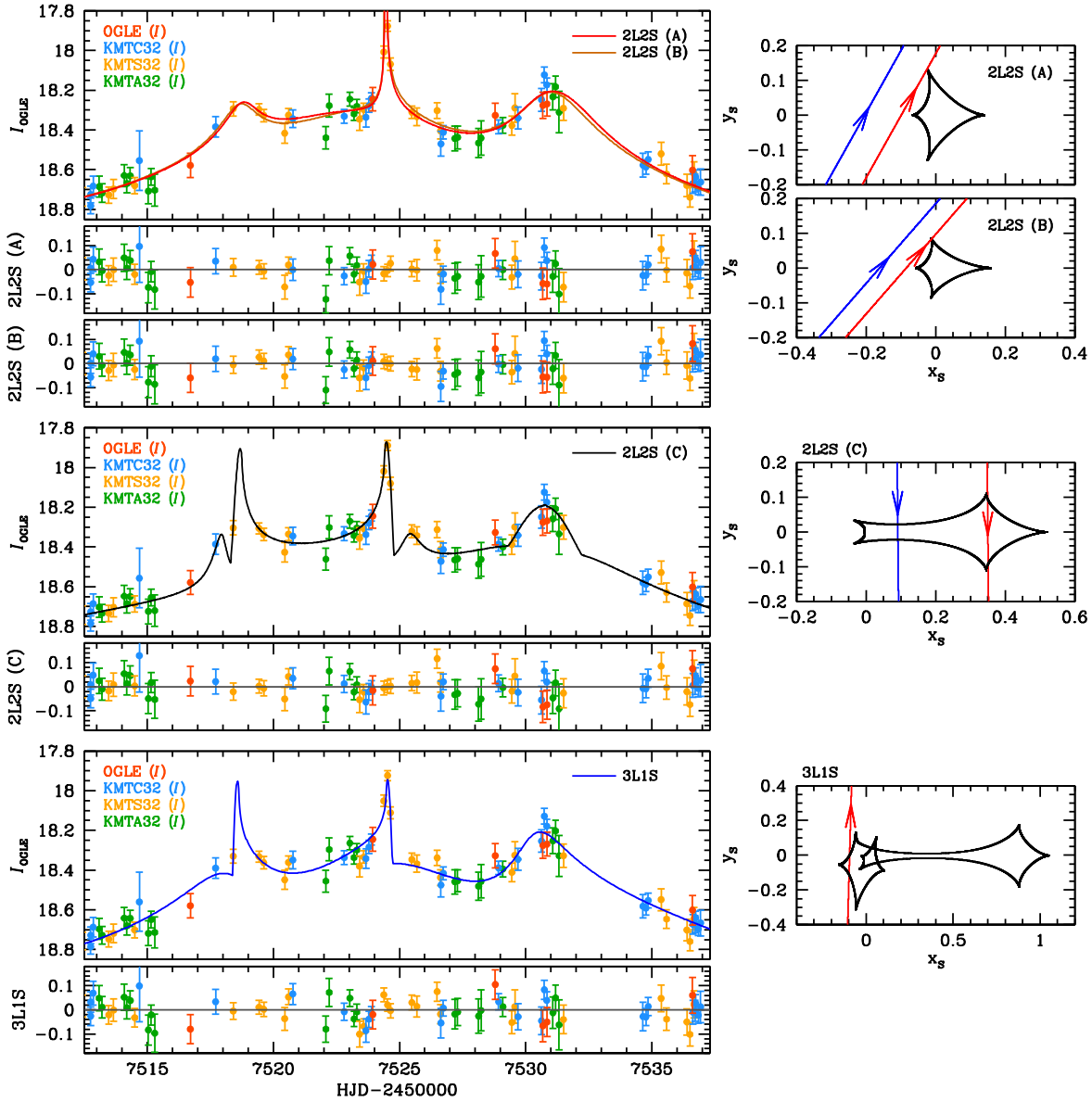

Figure 11. Light curves of OGLE-2016-BLG-0882 with degenerate models and their residuals. We also present the caustic geometries of each case.

Table 9
The Parameters of Degenerate Solutions for OGLE-2016-BLG-0882

Parameter	A: 2L2S	B: 2L2S	C: 2L2S	Parameter	3L1S
$\chi^2/N_{\rm data}$	1431.945/1436	1439.626/1436	1437.736/1436	$\chi^2/N_{\rm data}$	1471.948/1436
$\Delta\chi^2$	⋯ (best fit)	7.681	5.791	$\Delta\chi^2$	40.003
$t_{0,S1}$ [HJD′]	7520.424 ± 0.152	7521.433 ± 0.284	7521.529 ± 0.035	t_0	7524.747 ± 0.133
$u_{0,S1}$	0.086 ± 0.007	0.064 ± 0.006	0.350 ± 0.021	u_0	0.095 ± 0.007
t_E [days]	38.718 ± 2.156	55.660 ± 4.965	32.083 ± 0.923	t_E	54.345 ± 2.877
s	0.543 ± 0.012	2.651 ± 0.269	1.186 ± 0.012	s_1	1.523 ± 0.033
q	0.286 ± 0.017	0.568 ± 0.148	0.010 ± 0.001	q_1	0.074 ± 0.005
$\langle\log_{10}(q)\rangle$	−0.530 ± 0.024	−0.274 ± 0.111	−1.976 ± 0.042	$\langle\log_{10}(q_1)\rangle$	−1.156 ± 0.029
α	5.223 ± 0.018	5.430 ± 0.067	1.561 ± 0.007	α	4.740 ± 0.019
$t_{0,S2}$ [HJD′]	7524.833 ± 0.220	7526.798 ± 0.473	7530.741 ± 0.225	s_2	1.004 ± 0.002
$u_{0,S2}$	0.178 ± 0.014	0.122 ± 0.020	0.091 ± 0.012	q_2	0.011 ± 0.002
$q_{\rm flux}$	6.476 ± 1.186	5.081 ± 3.829	0.252 ± 0.031	$\langle\log_{10}(q_2)\rangle$	−1.972 ± 0.062
$\rho_{*,S1}$	<0.004	<0.004	0.003 ± 0.001	ψ	4.589 ± 0.029
$\rho_{*,S2}$	<0.047	<0.039	0.023 ± 0.015	ρ_* ($\times10^{-4}$)	11.194 ± 2.436

Note. HJD′ = HJD−2,450,000.0. For the $\rho_{*,S1}$ and $\rho_{*,S2}$ parameter, the cases with inequality signs are upper limits (i.e., 3σ), because we cannot robustly measure the source sizes.

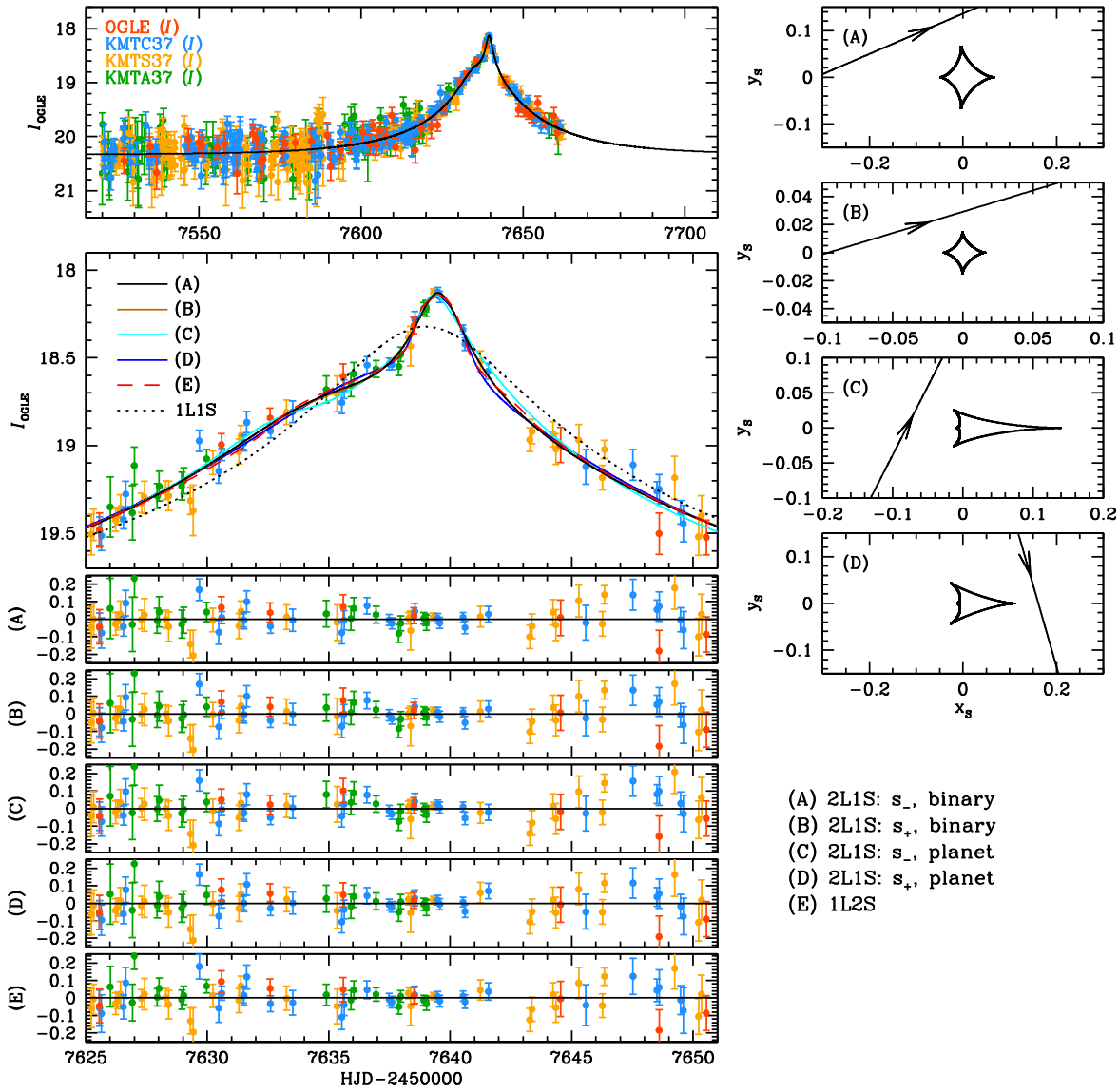

Figure 12. Light curves of OGLE-2016-BLG-1704 with degenerate models and their residuals. We also present the caustic geometries of each 2L1S case.

Table 10
The Parameters of Degenerate Solutions for OGLE-2016-BLG-1704

Case	2L1S: Binary		2L1S: Planet-like		1L2S	
Parameter	(A) s_-	(B) s_+	(C) s_-	(D) s_+	Parameter	(E)
$\chi^2/N_{\rm data}$	1791.049/1796	1791.171/1796	1793.005/1796	1804.127/1796	$\chi^2/N_{\rm data}$	1794.442/1796
$\Delta\chi^2$	⋯ (best fit)	0.122	1.956	13.078	$\Delta\chi^2$	3.393
t_0 [HJD′]	7638.124 ± 0.198	7638.611 ± 0.086	7638.207 ± 0.107	7638.209 ± 0.090	$t_{0,\rm S1}$ [HJD′]	7637.907 ± 0.193
u_0	0.125 ± 0.023	0.028 ± 0.010	0.155 ± 0.023	0.072 ± 0.011	$u_{0,\rm S1}$	0.238 ± 0.069
$t_{\rm E}$ [days]	39.040 ± 4.575	40.442 ± 6.261	32.127 ± 3.267	50.567 ± 7.298	$t_{\rm E}$ [days]	33.855 ± 4.459
s	0.363 ± 0.054	5.792 ± 0.443	0.723 ± 0.066	1.481 ± 0.051	$t_{0,\rm S2}$ [HJD′]	7639.517 ± 0.061
q	0.530 ± 0.240	0.076 ± 0.067	0.025 ± 0.016	0.020 ± 0.005	$u_{0,\rm S2}$	-0.006 ± 0.025
$\langle \log_{10} q \rangle$	-0.352 ± 0.202	-1.121 ± 0.283	-1.474 ± 0.177	-1.702 ± 0.112	$q_{\rm flux}$	0.059 ± 0.033
α [rad]	-0.408 ± 0.096	-0.303 ± 0.032	1.291 ± 0.031	5.185 ± 0.034	$\rho_{*,\rm S1}$	<0.525
ρ_*	<0.031	<0.017	<0.054	<0.021	$\rho_{*,\rm S2}$	<0.059

Note. HJD′ = HJD−2,450,000.0. We note that ρ_* is not measured for all cases. Thus, we present 3σ upper limits on the ρ_* values (i.e., $\rho_{*,\rm limit}$).

4. CMD Analysis

We cannot securely measure ρ_* for any of the four planetary events. We can determine only upper limits on the ρ_* values. However, we can apply the ρ_* distributions as constraints on the Bayesian analysis by including information on the angular source radius (θ_*) of each event in the analysis. Thus, we carry

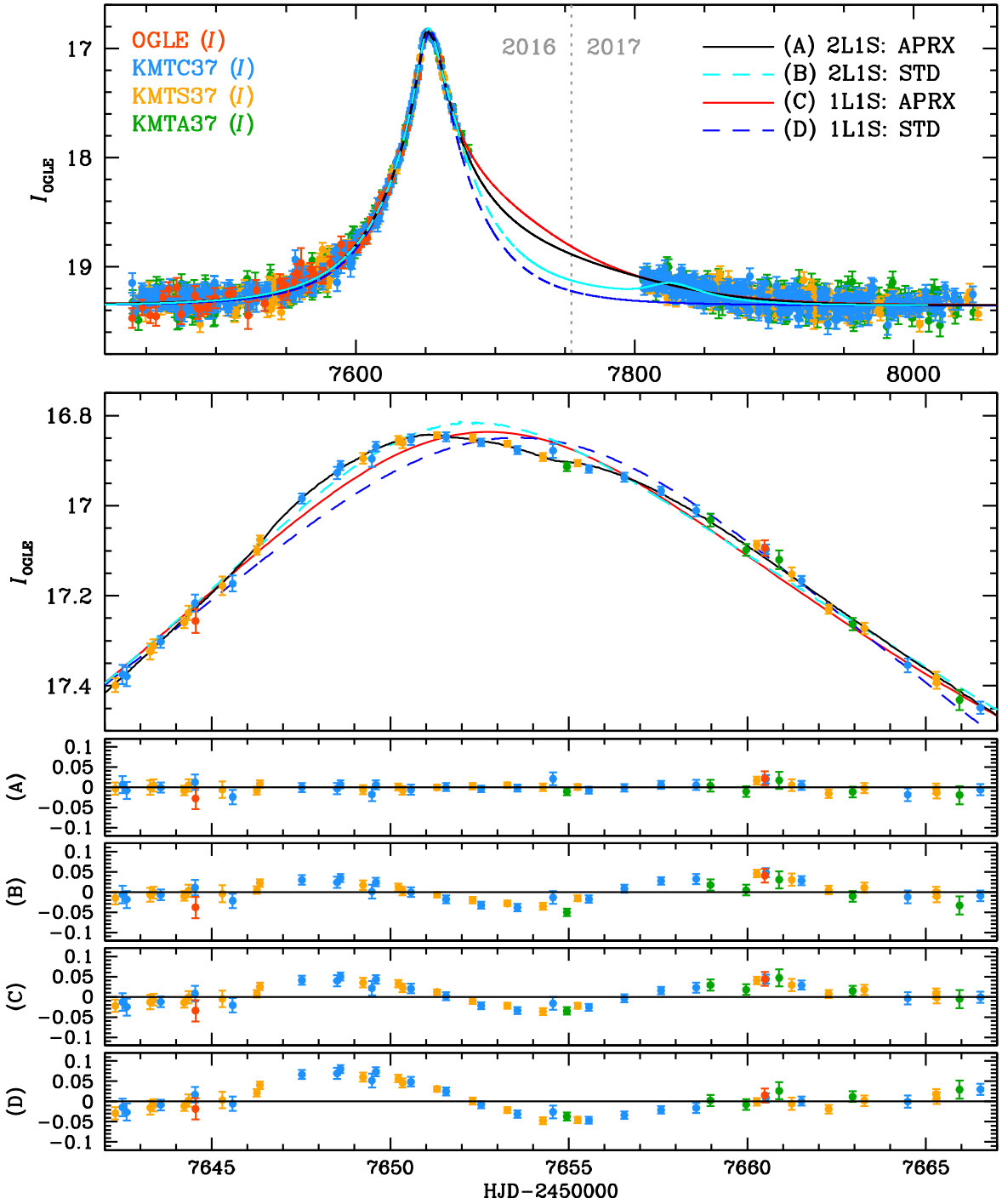

Figure 13. Light curves of OGLE-2016-BLG-1408 with 2L1S and 1L1S models. For the 2L1S and 1L1S models, we present both the STD and APRX cases.

out the CMD analysis to measure the θ_*. The basics of the CMD analysis are described in Yoo et al. (2004). In addition, the detailed procedures of the analysis are described in Shin et al. (2023b).

In Figure 18, we present the measured locations of the centroid of the red giant clump (RGC), the source, and the blend overlaid on the CMD of each event. Although the analysis is conducted based on the multiband KMTNet observations (i.e., I and V bands), we present them in the OGLE-III magnitude system because we determine the RGC based on the OGLE-III CMD (Szymański et al. 2011). The exception is KMT-2016-BLG-2321 because the OGLE-III CMD is not available for this event, so we present the uncalibrated/dereddend KMTNet magnitudes instead.

In Table 14, we present the results of the CMD analyses with the derived θ_* values. We also present the lower limits on the angular Einstein ring radii ($\theta_{\rm E}$) and lens-source relative proper motions ($\mu_{\rm rel}$). Indeed, the lower limit on $\mu_{\rm rel}$ (i.e., $\mu_{{\rm rel},+3\sigma} \equiv \theta_*/t_{\rm E}\rho_{*,+3\sigma}$) is a useful indicator to check the effect of the ρ_* constraint before proceeding with the actual Bayesian

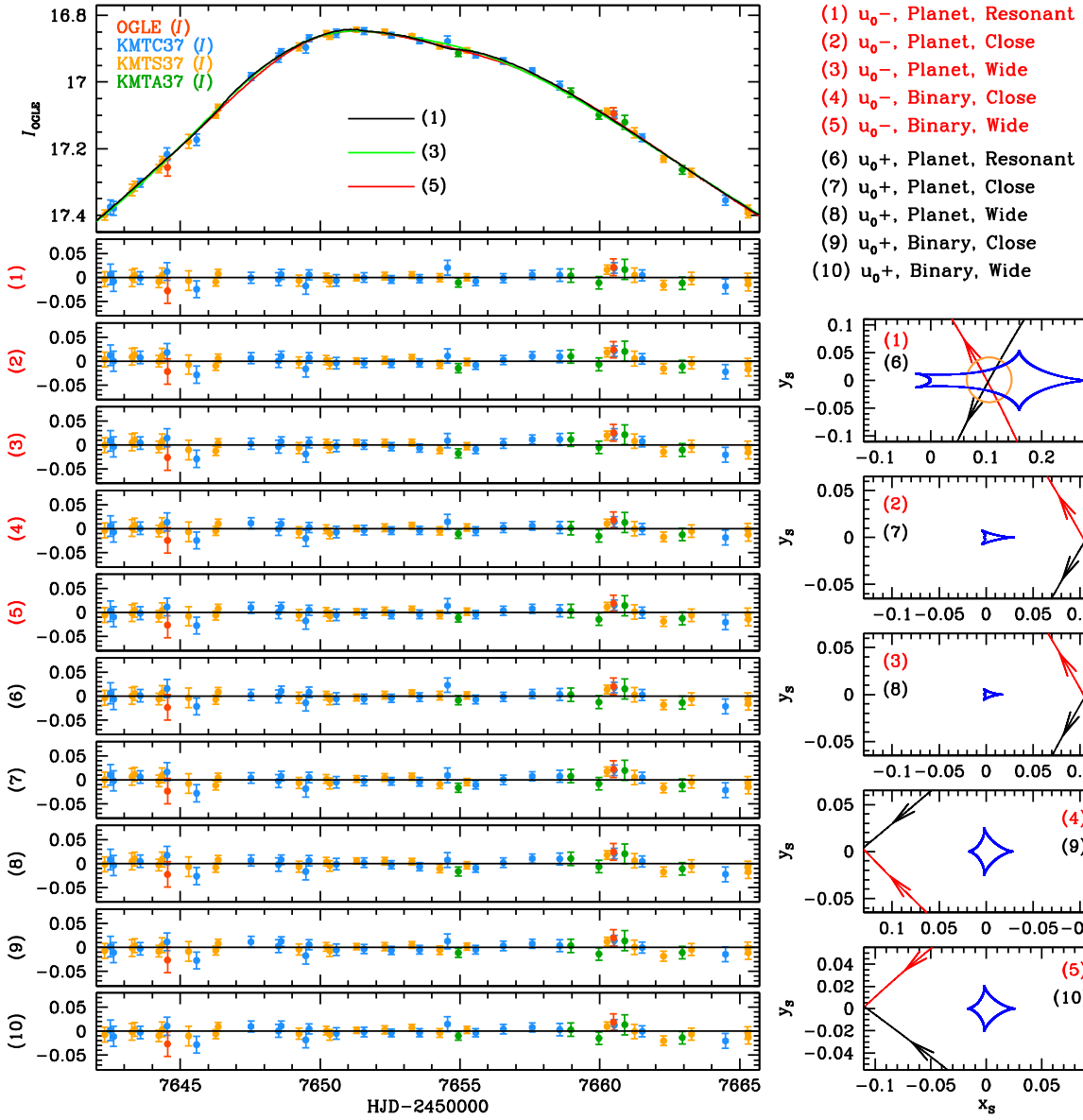

Figure 14. Comparison of 2L1S APRX models with their caustic geometries for OGLE-2016-BLG-1408.

analysis. In general, we expect $1 < \mu_{\rm rel}/{\rm mas\,yr^{-1}} < 10$. Hence, if the lower limit on $\mu_{\rm rel,+3\sigma} \lesssim 1\,{\rm mas\,yr^{-1}}$, we expect the ρ_* constraint to have little effect on the Bayesian result.

Note that, for KMT-2016-BLG-2321, we conduct an additional analysis to check our measurement of the source color because the quality of the V-band data is low. The V-band light curve has systematics because this event experienced severe extinction (i.e., $A_I \sim 3.88$), and the source is faint (i.e., $I_{\rm KMTNet} \sim 21.4$). Thus, we have checked our measurement using the source color estimation method (Bennett et al. 2008) and the Galactic bulge CMD (Holtzman et al. 1998) from the Hubble Space Telescope. We find that the estimated source color (i.e., $(V-I)_{0,\rm S}$=0.723 ± 0.055) is consistent with our measured color (i.e., $(V-I)_{0,\rm S}$ = 0.763 ± 0.092, or $(V-I)_{0,\rm S}$=0.752 ± 0.090) at the 1σ level. Hence, we conclude that our measurement is reliable despite the obstacles.

5. Planet Properties

The lens properties such as the mass of the lens system ($M_{\rm L}$), distance to the lens ($D_{\rm L}$), projected separation between lens components ($a_\perp$), and lens-source relative proper motion ($\mu_{\rm rel}$) can be determined from

$$M_{\rm L} = \frac{\theta_{\rm E}}{\kappa\,|\,\boldsymbol{\pi}_{\rm E}\,|}, \quad D_{\rm L} = \frac{\rm au}{\theta_{\rm E}\,|\,\boldsymbol{\pi}_{\rm E}\,|\,+\pi_{\rm S}},$$
$$a_\perp = sD_{\rm L}\theta_{\rm E}, \quad \mu_{\rm rel} = \frac{\theta_{\rm E}}{t_{\rm E}}, \qquad (1)$$

where $\kappa = 8.144\,{\rm mas}\,M_\odot^{-1}$, and $\pi_{\rm S}$ is the parallax of the source defined as $\pi_{\rm S} \equiv {\rm au}/D_{\rm S}$ ($D_{\rm S}$ is distance to the source). As shown in Equation (1), two observables (i.e., $\theta_{\rm E}$ and $|\boldsymbol{\pi}_{\rm E}|$) need to be measured to directly determine the lens properties. These observables may be measured from the finite-source and microlens-parallax effects, respectively. However, for the planetary events in this work, we do not have measurements

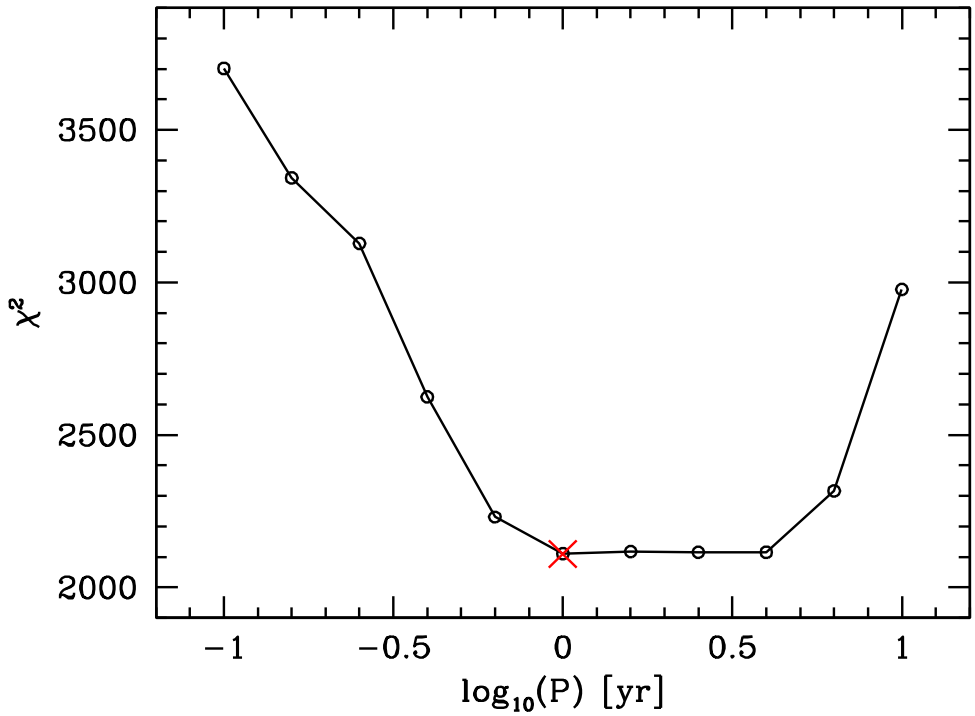

Figure 15. Test of the xallarap effect for OGLE-2016-BLG-1408, which shows χ^2 value for each rotation period (P) of the binary source system. The red cross indicates the best-fit χ^2 of the APRX model, which is equal to 1 yr.

Table 11
The Parameters of 2L1S APRX Models for OGLE-2016-BLG-1408

Case	Planet			Binary	
Parameter	Resonant (u_0-)	Close (u_0-)	Wide (u_0-)	Close (u_0-)	Wide (u_0-)
$\chi^2/N_{\rm data}$	2109.666/2124	2119.292/2124	2121.676/2124	2110.571/2124	2111.403/2124
$\Delta\chi^2$	⋯ (best fit)	9.626	12.010	0.905	1.737
t_0 [HJD′]	7653.474 ± 0.048	7653.458 ± 0.051	7653.432 ± 0.055	7653.763 ± 0.103	7653.127 ± 0.070
u_0	−0.089 ± 0.002	−0.089 ± 0.002	−0.090 ± 0.003	−0.090 ± 0.003	−0.073 ± 0.005
$t_{\rm E}$ [days]	96.686 ± 2.217	96.302 ± 2.287	95.185 ± 2.331	95.874 ± 2.872	117.147 ± 8.281
s	1.083 ± 0.005	0.701 ± 0.094	1.742 ± 0.235	0.263 ± 0.018	5.400 ± 0.586
q ($\times10^{-4}$)	18.382 ± 2.461	47.894 ± 40.051	65.010 ± 37.037	⋯	⋯
q	⋯	⋯	⋯	0.275 ± 0.071	0.571 ± 0.199
$\langle\log_{10} q\rangle$	−2.752 ± 0.061	−2.186 ± 0.216	−2.187 ± 0.171	−0.525 ± 0.093	−0.229 ± 0.136
α [rad]	4.200 ± 0.018	4.176 ± 0.020	4.179 ± 0.019	5.522 ± 0.043	2.453 ± 0.033
ρ_*	0.040 ± 0.003	<0.047	<0.046	<0.044	<0.034
$\pi_{{\rm E},N}$	0.196 ± 0.059	0.203 ± 0.063	0.228 ± 0.056	0.183 ± 0.060	0.180 ± 0.058
$\pi_{{\rm E},E}$	−0.247 ± 0.012	−0.244 ± 0.014	−0.242 ± 0.013	−0.241 ± 0.014	−0.198 ± 0.012
	Resonant (u_0+)	Close (u_0+)	Wide (u_0+)	Close (u_0+)	Wide (u_0+)
$\chi^2/N_{\rm data}$	2110.464/2124	2117.795/2124	2119.989/2124	2114.903/2124	2115.099/2124
$\Delta\chi^2$	0.798	8.129	10.323	5.237	5.433
t_0 [HJD′]	7653.541 ± 0.055	7653.510 ± 0.063	7653.522 ± 0.069	7653.637 ± 0.142	7653.124 ± 0.120
u_0	0.093 ± 0.003	0.093 ± 0.003	0.093 ± 0.003	0.087 ± 0.007	0.065 ± 0.007
$t_{\rm E}$ [days]	97.872 ± 2.143	96.546 ± 1.952	97.192 ± 1.903	100.772 ± 6.035	134.427 ± 9.191
s	1.086 ± 0.005	0.702 ± 0.070	1.746 ± 0.174	0.241 ± 0.021	6.090 ± 0.751
q($\times10^{-4}$)	17.348 ± 2.181	48.054 ± 30.889	63.992 ± 26.388	⋯	⋯
q	⋯	⋯	⋯	0.350 ± 0.112	0.797 ± 0.213
$\langle\log_{10} q\rangle$	−2.781 ± 0.058	−2.151 ± 0.168	−2.194 ± 0.147	−0.429 ± 0.112	−0.285 ± 0.167
α [rad]	2.054 ± 0.017	2.092 ± 0.018	2.075 ± 0.016	0.708 ± 0.041	3.805 ± 0.044
ρ_*	0.041 ± 0.002	<0.046	<0.044	<0.040	<0.033
$\pi_{{\rm E},N}$	0.158 ± 0.050	0.166 ± 0.046	0.173 ± 0.045	0.064 ± 0.080	0.074 ± 0.048
$\pi_{{\rm E},E}$	−0.246 ± 0.010	−0.246 ± 0.010	−0.241 ± 0.011	−0.258 ± 0.011	−0.182 ± 0.013

Note. HJD′ = HJD–2,450,000.0. For the ρ_* parameter, the cases with the inequality signs are upper limits on the ρ_* (i.e., 3σ) because we cannot robustly measure ρ_*.

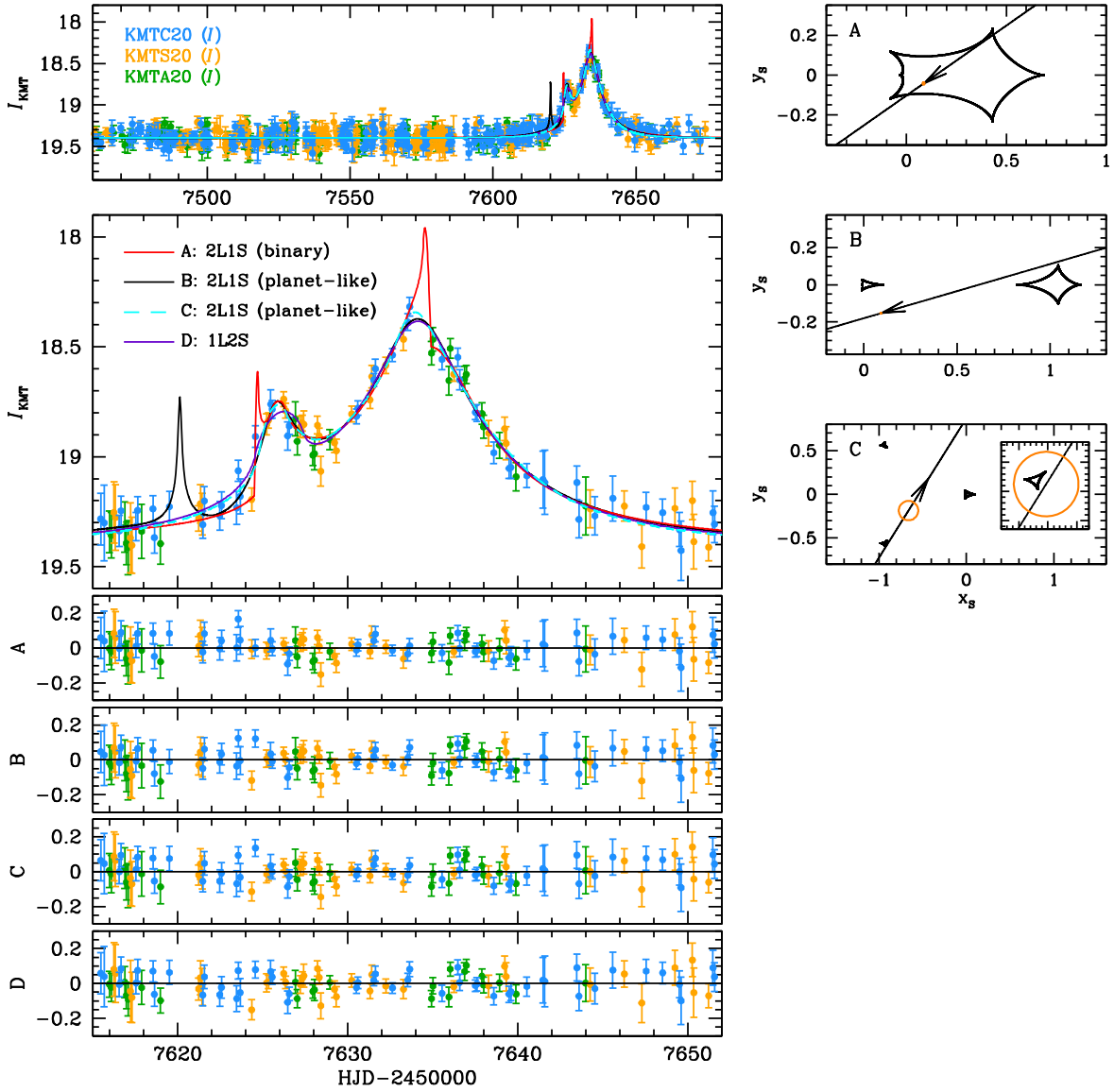

Figure 16. Light curves of KMT-2016-BLG-2399 with 2L1S and 1L2S models. Note model B has a sharp feature near HJD′ ∼ 7620 that lacks data coverage. We also present the caustic geometries of the 2L1S models.

Table 12
The Parameters of 2L1S and 1L2S Models for KMT-2016-BLG-2399

Parameter	A: 2L1S	B: 2L1S	C: 2L1S	Parameter	D: 1L2S
$\chi^2/N_{\rm data}$	630.708/632	640.907/632	645.397/632	$\chi^2/N_{\rm data}$	644.879/632
$\Delta\chi^2$	⋯ (best fit)	10.199	14.689	$\Delta\chi^2$	14.171
t_0 [HJD′]	7633.696 ± 0.088	7633.798 ± 0.067	7633.450 ± 0.090	$t_{0,S1}$ [HJD′]	7625.980 ± 0.097
u_0	0.084 ± 0.007	0.173 ± 0.020	0.462 ± 0.061	$u_{0,S1}$	0.002 ± 0.085
t_E [days]	19.173 ± 1.219	13.168 ± 1.265	7.970 ± 0.587	t_E [days]	11.171 ± 1.991
s	1.229 ± 0.016	1.646 ± 0.062	0.607 ± 0.024	$t_{0,S2}$ [HJD′]	7634.150 ± 0.068
q	0.057 ± 0.009	0.030 ± 0.006	0.049 ± 0.008	$u_{0,S2}$	0.221 ± 0.150
$\langle\log_{10} q\rangle$	−1.227 ± 0.068	−1.580 ± 0.104	−1.303 ± 0.069	$q_{\rm flux}$	12.943 ± 2.610
α [rad]	2.530 ± 0.017	2.858 ± 0.015	−1.011 ± 0.031	$\rho_{*,S1}$	<0.430
ρ_*	0.006 ± 0.003	<0.038	0.111 ± 0.023	$\rho_{*,S2}$	<1.038

Note. HJD′ = HJD−2,450,000.0. For the ρ_* parameter, the cases with the inequality signs are upper limits on the ρ_* (i.e., 3σ) because we cannot robustly measure ρ_*.

of either observable. Thus, we conduct a Bayesian analysis to estimate the lens properties for the new planetary systems. We follow the formalism and procedures of the Bayesian analysis described in Shin et al. (2023a, 2023b).

In Table 15, we present the lens properties estimated from the Bayesian analyses for each event. Note that we apply the t_E and ρ_* distribution constraints to the Bayesian analyses for all planetary events. For each event, we present several lens

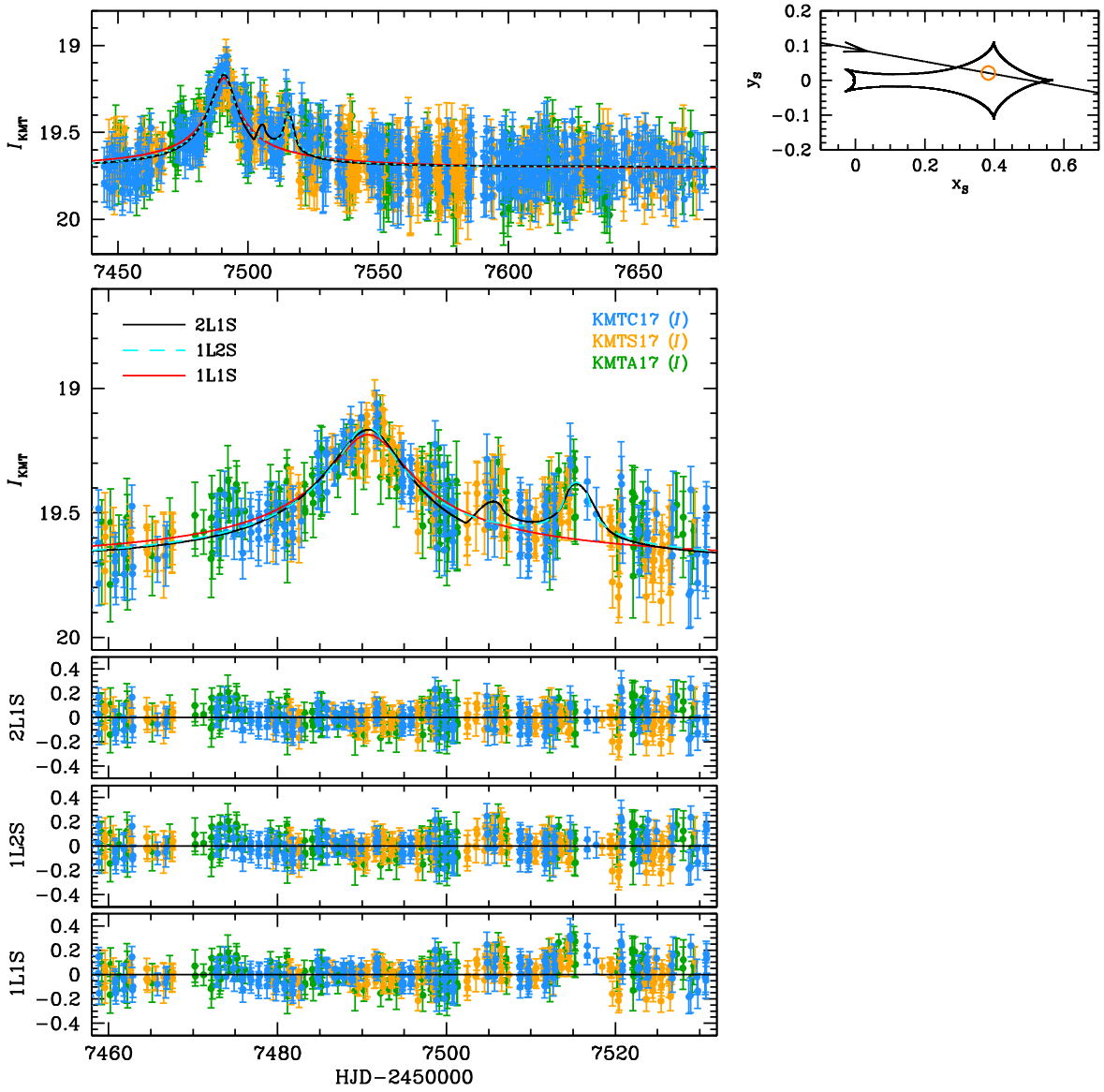

Figure 17. Light curves of KMT-2016-BLG-2473 with 2L1S and 1L2S models, their residuals, and the 2L1S caustic geometry.

Table 13
The Parameters of 2L1S and 1L2S Models for KMT-2016-BLG-2473

Parameter	2L1S	Parameter	1L2S
$\chi^2/N_{\rm data}$	1529.729/1535	$\chi^2/N_{\rm data}$	1540.057/1535
$\Delta\chi^2$	⋯ (best fit)	$\Delta\chi^2$	10.328
t_0 [HJD′]	7491.437 ± 0.206	$t_{0,\rm S1}$ [HJD′]	7515.409 ± 0.322
u_0	0.088 ± 0.009	$u_{0,\rm S1}$	0.033 ± 0.036
$t_{\rm E}$ [days]	47.179 ± 4.634	$t_{\rm E}$ [days]	51.742 ± 11.156
s	1.217 ± 0.026	$t_{0,\rm S2}$ [HJD′]	7490.605 ± 0.160
q	0.011 ± 0.003	$u_{0,\rm S2}$	0.103 ± 0.043
$\langle\log_{10} q\rangle$	−1.967 ± 0.137	$q_{\rm flux}$	7.663 ± 1.829
α [rad]	0.178 ± 0.012	$\rho_{*,\rm S1}$	<0.116
ρ_*	0.019 ± 0.006	$\rho_{*,\rm S2}$	<0.275

Note. HJD′ = HJD−2,450,000.0. For the ρ_* parameters, the cases with the inequality signs are upper limits on the ρ_* (i.e., 3σ) because we cannot robustly measure ρ_*.

properties because of the degenerate solutions. Thus, we present "adopted" values for ease of cataloging, which are weighted average values described in Jung et al. (2023).

5.1. OGLE-2016-BLG-1598

The planetary lens system of this event consists of a sub-Jupiter-mass planet ($M_{\rm planet}\sim 0.37$ or $\sim 0.70\,M_{\rm J}$) orbiting an early M-dwarf host star ($M_{\rm host}\sim 0.55$, $M_\odot$) with a projected separation of ∼2.5 or ∼1.9 au. This planetary system is located at a distance of ∼5.9 kpc from us. The properties of the planetary system are those of a typical microlensing planet, i.e., a Jupiter-class planet orbiting an M-dwarf host beyond the snow line (Ida & Lin 2005; Kennedy & Kenyon 2008).

5.2. OGLE-2016-BLG-1800

For this event, the lens system is composed of a super Jupiter-mass planet ($M_{\rm planet}\sim 2.49$ or $\sim 2.77\,M_{\rm J}$) and an M-dwarf host star ($M_{\rm host}\sim 0.41$, $M_\odot$). The planet orbits the host with a projected separation of ∼1.5 or ∼2.6 au. The system is located at a distance of ∼6.5 kpc from us. This planetary system is also one that is typical for microlensing planets.

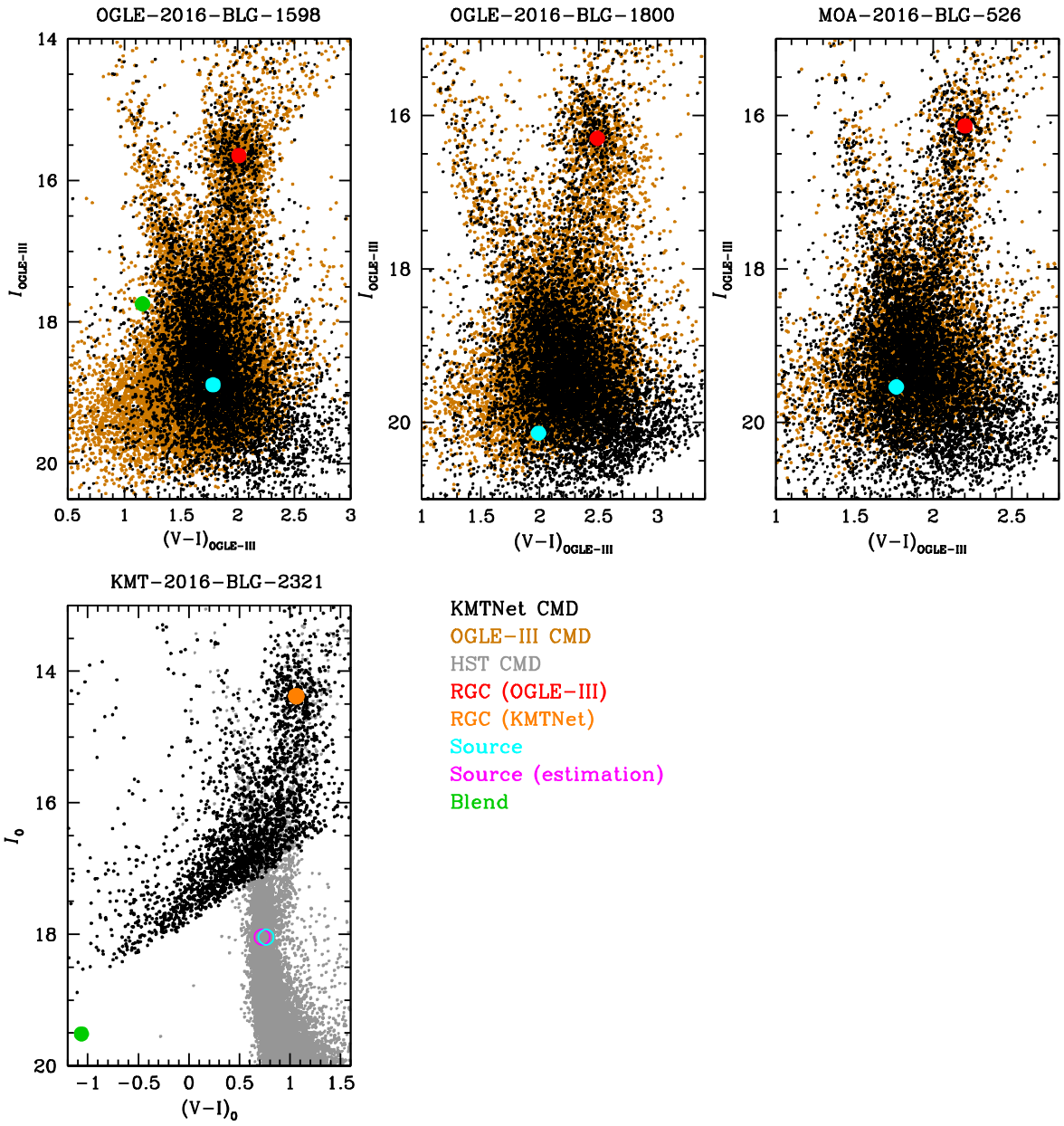

Figure 18. Color–magnitude diagrams (CMDs) of four planetary events.

5.3. MOA-2016-BLG-526

Despite several solutions, the Bayesian results indicate that the properties of the host star are consistent, i.e., it is an M-dwarf star with the mass of $\sim 0.4\,M_{\odot}$. However, because of the variation in mass ratios for different solutions, the planet could be either a sub-Neptune-mass or Neptune-class planet (see Table 15). This planet orbits the host with a projected separation $a_{\perp} \sim 2$ au. This planetary system is located at a distance of $\sim$6.9 kpc from us.

5.4. KMT-2016-BLG-2321

Bayesian results show that the lens system of this event consists of a Jupiter-class planet ($M_{\rm planet} \sim 0.94$ or $\sim 0.98\,M_{\rm J}$) orbiting a mid-K-type host star ($M_{\rm host} \sim 0.73$, $M_{\odot}$) with a projected separation of $\sim$3.4 or $\sim$3.8 au. The system is located at the distance of $\sim$3.6 or $\sim$3.5 kpc.

Note that, for this event, the constraints from the ρ_* distributions have a major effect on the posteriors, in contrast to the other cases presented above. Indeed, we can expect the effect of the ρ_* constraints to be significant as described in Section 4. Specifically, for this event, $\mu_{{\rm rel},+3\sigma} \sim 4$ mas yr^{-1}, which is much larger than 1 mas yr^{-1}. Meanwhile, for the other events, the effects of the ρ_* constraints were minor, as would be expected from lower limits of $\mu_{{\rm rel},+3\sigma} \lesssim 1$ mas yr^{-1} (see Table 14).

6. Summary and Discussion

Through our systematic planetary anomaly search, we found four hidden planets and seven planet candidates in the 2016 KMTNet subprime fields. The properties of these new planetary systems are those of typical microlensing planets, i.e., giant planets orbiting M-dwarf host stars beyond their

Table 14
CMD Analyses of Planetary Events

Event Case	$(V-I)_{\rm RGC}$ $I_{\rm RGC}$	$(V-I)_{0,\rm RGC}$ $I_{0,\rm RGC}$	$(V-I)_{\rm S}$ $I_{\rm S}$	$(V-I)_{0,\rm S}$ $I_{0,\rm S}$	$(V-I)_{\rm B}$ $I_{\rm B}$	θ_* (μas)	$\theta_{\rm E}$ (mas)	$\mu_{\rm rel}$ (mas yr^{-1})
OB161598								
Outer	2.012	1.060	1.785 ± 0.022	0.833 ± 0.055	1.161 ± 0.008	1.080 ± 0.065	>0.013	>0.127
	15.648	14.385	18.886 ± 0.006	17.623 ± 0.006	17.743 ± 0.004	⋯	⋯	⋯
Inner	2.012	1.060	1.784 ± 0.022	0.832 ± 0.055	1.165 ± 0.008	1.068 ± 0.065	>0.018	>0.175
	15.648	14.385	18.907 ± 0.006	17.645 ± 0.006	17.736 ± 0.004	⋯	⋯	⋯
OB161800								
s_-	2.489	1.060	1.991 ± 0.058	0.562 ± 0.076	⋯	0.591 ± 0.046	>0.010	>0.185
	16.296	14.450	20.139 ± 0.012	18.294 ± 0.012	⋯	⋯	⋯	⋯
s_+	2.489	1.060	1.991 ± 0.059	0.562 ± 0.078	⋯	0.611 ± 0.048	>0.009	>0.158
	16.296	14.450	20.066 ± 0.012	18.220 ± 0.012	⋯	⋯	⋯	⋯
MB16526								
s_- (A)	2.203	1.060	1.767 ± 0.015	0.624 ± 0.052	⋯	0.716 ± 0.039	>0.102	>1.918
	16.136	14.611	19.536 ± 0.007	18.011 ± 0.007	⋯	⋯	⋯	
s_- (B)	2.203	1.060	1.763 ± 0.015	0.620 ± 0.052	⋯	0.713 ± 0.039	>0.079	>1.488
	16.136	14.611	19.538 ± 0.007	18.012 ± 0.007	⋯	⋯	⋯	
s_- (C)	2.203	1.060	1.767 ± 0.015	0.624 ± 0.052	⋯	0.728 ± 0.040	>0.081	>1.552
	16.136	14.611	19.501 ± 0.007	17.976 ± 0.007	⋯	⋯	⋯	
s_+ (A)	2.203	1.060	1.762 ± 0.015	0.619 ± 0.052	⋯	0.709 ± 0.039	>0.101	>1.891
	16.136	14.611	19.548 ± 0.007	18.023 ± 0.007	⋯	⋯	⋯	
s_+ (B)	2.203	1.060	1.764 ± 0.015	0.621 ± 0.052	⋯	0.717 ± 0.039	>0.102	>1.934
	16.136	14.611	19.527 ± 0.007	18.002 ± 0.007	⋯	⋯	⋯	
KB162321[a]								
Outer	3.863	1.060	3.566 ± 0.077	0.763 ± 0.092	1.740 ± 0.238	0.825 ± 0.085	>0.563	>3.617
	17.762	14.378	21.425 ± 0.012	18.041 ± 0.012	22.898 ± 0.151	⋯	⋯	⋯
Inner	3.863	1.060	3.555 ± 0.075	0.752 ± 0.090	1.719 ± 0.240	0.818 ± 0.083	>0.645	>4.137
	17.762	14.378	21.417 ± 0.012	18.033 ± 0.012	22.938 ± 0.156	⋯	⋯	⋯

Notes. We use the abbreviation for event names, e.g., OGLE-2016-BLG-1598 is abbreviated as OB161598.
[a] For KB162321, we note that the V and I magnitudes are in units of the instrumental scale of the KMTNet. Because there is no available OGLE-III catalog for this event, the magnitude system is not scaled to the OGLE-III.

Table 15
Lens Properties of Planetary Events

Event	Constraints	Case	$M_{\rm host}$ ($M_\odot$)	$M_{\rm planet}$ ($M_{\rm J}/M_{\rm N}/M_\oplus$)	$D_{\rm L}$ (kpc)	$a_\perp$ (au)	$\mu_{\rm rel}$ (mas yr^{-1})	Gal. Mod.	χ^2
OB161598	$t_{\rm E}+\rho_*$	outer	$0.55^{+0.34}_{-0.32}$	$0.37^{+0.31}_{-0.30}\,M_{\rm J}$	$5.91^{+1.28}_{-2.27}$	$2.51^{+0.89}_{-0.92}$	$4.65^{+2.76}_{-1.75}$	0.714	1.000
		inner	$0.55^{+0.34}_{-0.32}$	$0.70^{+0.48}_{-0.46}\,M_{\rm J}$	$5.91^{+1.28}_{-2.27}$	$1.92^{+0.67}_{-0.70}$	$4.63^{+2.77}_{-1.74}$	1.000	0.015
Adopted			0.55 ± 0.32	$0.38 \pm 0.30\,M_{\rm J}$	5.91 ± 1.74	2.50 ± 0.88	4.65 ± 2.21		
OB161800	$t_{\rm E}+\rho_*$	s_-	$0.41^{+0.33}_{-0.26}$	$2.49^{+2.13}_{-1.65}\,M_{\rm J}$	$6.47^{+1.14}_{-1.65}$	$1.49^{+0.59}_{-0.56}$	$6.36^{+2.90}_{-2.33}$	1.000	1.000
		s_+	$0.40^{+0.33}_{-0.26}$	$2.77^{+2.67}_{-1.83}\,M_{\rm J}$	$6.49^{+1.14}_{-1.63}$	$2.60^{+1.05}_{-0.97}$	$6.43^{+2.93}_{-2.35}$	0.850	0.632
Adopted			0.41 ± 0.22	$2.59 \pm 1.46\,M_{\rm J}$	6.48 ± 1.03	1.88 ± 0.51	6.38 ± 1.94		
MB16526	$t_{\rm E}+\rho_*$	s_- (A)	$0.37^{+0.34}_{-0.23}$	$1.27^{+1.21}_{-0.87}\,M_{\rm N}$	$6.92^{+1.29}_{-1.98}$	$1.99^{+0.79}_{-0.71}$	$6.09^{+2.84}_{-2.19}$	0.908	1.000
		s_- (B)	$0.37^{+0.34}_{-0.23}$	$0.84^{+0.81}_{-0.60}\,M_{\rm N}$	$6.94^{+1.29}_{-1.98}$	$2.00^{+0.81}_{-0.73}$	$6.06^{+2.85}_{-2.22}$	0.913	0.999
		s_- (C)	$0.36^{+0.34}_{-0.23}$	$1.12^{+1.14}_{-0.77}\,M_{\rm N}$	$6.95^{+1.28}_{-1.96}$	$2.01^{+0.81}_{-0.72}$	$6.11^{+2.86}_{-2.22}$	1.000	0.896
		s_+ (A)	$0.38^{+0.34}_{-0.23}$	$0.44^{+0.61}_{-0.30}\,M_{\rm N}$	$6.90^{+1.29}_{-1.98}$	$2.27^{+0.89}_{-0.79}$	$6.15^{+2.81}_{-2.15}$	0.902	0.652
		s_+ (B)	$0.37^{+0.34}_{-0.23}$	$0.34^{+0.70}_{-0.22}\,M_{\rm N}$	$6.91^{+1.29}_{-1.98}$	$2.20^{+0.86}_{-0.77}$	$6.17^{+2.82}_{-2.17}$	0.918	0.596
Adopted			0.37 ± 0.13	$0.87 \pm 0.38\,M_{\rm N}$	6.93 ± 0.75	2.07 ± 0.35	6.11 ± 1.15		
KB162321	$t_{\rm E}+\rho_*$	outer	$0.73^{+0.41}_{-0.36}$	$0.94^{+0.55}_{-0.57}\,M_{\rm J}$	$3.64^{+1.84}_{-1.60}$	$3.41^{+0.96}_{-1.20}$	$5.78^{+2.79}_{-1.55}$	0.992	1.000
		inner	$0.73^{+0.43}_{-0.36}$	$0.98^{+0.59}_{-0.59}\,M_{\rm J}$	$3.49^{+1.77}_{-1.54}$	$3.81^{+1.10}_{-1.36}$	$6.15^{+2.78}_{-1.62}$	1.000	0.717
Adopted			0.73 ± 0.28	$0.95 \pm 0.41\,M_{\rm J}$	3.58 ± 1.22	3.58 ± 0.81	5.94 ± 1.56		

Note. For the planet mass, we present the value in Jupiter ($M_{\rm J}$), Neptune ($M_{\rm N}$), or Earth ($M_\oplus$) masses as appropriate.

snow lines. Although these new planets show typical properties discovered by the microlensing method, these are complementary planet samples compared to samples discovered by other detection methods because of the different detection sensitivities of each method (Clanton & Gaudi 2014a, 2014b; Shin et al. 2019).

Table 16
Planetary Events Discovered or Recovered by the KMTNet AnomalyFinder in 2016

Event Name	KMT Name	KMT Field	$\log_{10}(q)$	s	Degeneracy	Method	References
KB161105	...	subprime	−5.19	1.14	i/o, c/w	AF	Zang et al. (2023)
OB160007	KB161991	prime	−5.17	2.83	...	AF	Zang et al. (2024)
OB161195[a]	KB160372	prime	−4.34	0.99	c/w, ecliptic	by eye	Gould et al. (2023)
OB161850	KB161307	prime	−4.00	0.80	i/o, ecliptic	AF	Shin et al. (2023b)
OB161598	KB160696	subprime	−3.19	0.96	i/o	AF	This work
KB162321	...	subprime	−2.91	1.04	i/o	AF	This work
OB161067	KB161453	subprime	−2.84	0.81	s-degen., ecliptic	by eye	Calchi Novati et al. (2019)
OB161093	KB161345	subprime	−2.84	1.02	ecliptic	by eye	Shin et al. 2022
MB16319	KB161816	prime	−2.41	0.82	i/o	by eye	Han et al. (2018)
KB162397	...	subprime	−2.40	1.15	c/w	by eye	Han et al. (2020b)
MB16532	KB160506	prime	−2.39	0.65	c/w	AF	Shin et al. (2023b)
KB161836	...	prime	−2.35	1.30	c/w, ecliptic	by eye	Yang et al. (2020)
OB161800	KB160781	subprime	−2.24	0.69	c/w	AF	This work
KB162364	...	subprime	−2.12	1.17	...	by eye	Han et al. (2020b)
OB161227	KB161089	subprime	−2.10	3.68	i/o	by eye	Han et al. (2020a)
MB16227	KB160622	prime	−2.03	0.93	...	by eye	Koshimoto et al. (2017)
OB160596	KB161677	prime	−1.93	1.08	...	by eye	Mróz et al. (2017)
KB162605	...	prime	−1.92	0.94	...	by eye	Ryu et al. (2021)
OB161190	KB160113	prime	−1.84	0.60	ecliptic	by eye	Ryu et al. (2018)
KB161397	...	subprime	−1.80	1.68	c/w	by eye	Zang et al. (2018)
OB161635	KB160269	prime	−1.59	0.59	c/w	AF	Shin et al. (2023b)
OB160263	KB161515	subprime	−1.51	4.72	α-degen.	by eye	Han et al. (2017a)
KB161107	...	subprime	−1.44	0.35	c/w	by eye	Hwang et al. (2019)
MB16526	KB161611	subprime	−3.75	0.94	c/w, i/o	AF	This work
KB160625	...	prime	−3.63	0.74	c/w	AF	Shin et al. (2023b)
OB160613[b]	KB160017	prime	−2.26	1.06	c/w	by eye	Han et al. (2017b)
KB161751	...	prime	−2.19	1.05	c/w	AF	Shin et al. (2023b)
KB161855[c]	...	prime	−1.61	3.80	c/w, α, offset, 1L2S	AF	Shin et al. (2023b)
KB160212	...	prime	−1.43	0.83	c/w	by eye	Hwang et al. (2018)
KB161820	...	prime	−0.95	1.40	...	by eye	Jung et al. (2018)
KB162142[c]	...	prime	−0.69	0.97	c/w	by eye	Jung et al. (2018)

Notes. The horizontal line separates planets expected to be part of the final statistical sample and those whose mass ratios are likely too uncertain or too large to be included. In the column of "Degeneracy," we present the type of degeneracies for the solutions: "c/w," "i/o," "ecliptic," "offset," "α," and "1L2S" indicate the close/wide (c/w) degeneracy, inner/outer (i/o) degeneracy, ecliptic degeneracy of the microlens-parallax effect, offset-degeneracy, α-degeneracy (see Shin et al. 2023a), and 2L1S/1L2S degeneracy, respectively. Note that "s-degen." indicates small/large s degeneracy (this is different from "c/w"; see Calchi Novati et al. 2019).
[a] For OB161195, the properties of this planetary system were reported by Shvartzvald et al. (2017) and Bond et al. (2017). However, we adopt $\log_{10}(q)$ and s values from Gould et al. (2023), which reanalyze the event and measure a more precise mass ratio.
[b] For OB160613, the event was caused by a lens system consisting of a planet and binary host stars.
[c] For KB161855 and KB162142, these are planet candidates.

In Table 16, we present all planetary events observed in 2016, including the new planets of this work. Both the by-eye and the AF methods were used to identify these planets. This work contributes 31% of the total number of planets discovered in the 2016 KMTNet subprime fields. Similarly to the contribution of this work, Shin et al. (2023b) reported five planets, which contributed 33% of the total number of planets discovered in 2016 in the prime fields. Hence, for the high- and low-cadence fields, we found a similar fraction of hidden planets.

Despite the number of new planets in both fields being similar, the number of new planet candidates shows a big difference. Shin et al. (2023b) found only one planet candidate in the high-cadence fields. By contrast, we found seven planet candidates in the low-cadence fields. These events are treated as planet candidates because we cannot resolve the binary/planet or 2L1S/1L2S degeneracy, which is caused by nonoptimal coverage of the anomalies. This fact clearly shows the importance of high-cadence observations to conclusively claim planet detections.

Now that we have finished the systematic search work for both prime and subprime fields observed in 2016, 2018, and 2019, in Figure 19, we present the cumulative number of planets discovered by the AF and by eye as functions of $\log_{10}(q)$. For each year, we find that 86%(=6/7), 55%(=6/11), and 75%(=9/12) of total planetary events having $\log_{10}(q) < -3.0$ were identified by the AF method, respectively. Combining the three seasons, a 70% (=21/30) of planetary systems in the region of $\log_{10}(q) < -3.0$ were discovered by the AF method rather than by eye. This is a remarkable result. Indeed, a total of 53 planetary events were identified by the conventional method (i.e., by eye) in the 2016, 2018, and 2019 seasons. However, only 17%(=9/53) of those planetary systems have $\log_{10}(q) < -3.0$. This lack of planet abundance in the region of $\log_{10}(q) < -3.0$ is unexpected considering the fact that microlensing detections are only weakly dependent on the mass of the planet ($\propto q^{1/2}$), and KMTNet's near-continuous observations should easily capture, e.g., the ∼8 hr signals due to $\log_{10}(q) \sim -4$ planets. However, this investigation simply shows that most of the planetary systems having $\log_{10}(q) < -3.0$ were just buried in the archive and missed by

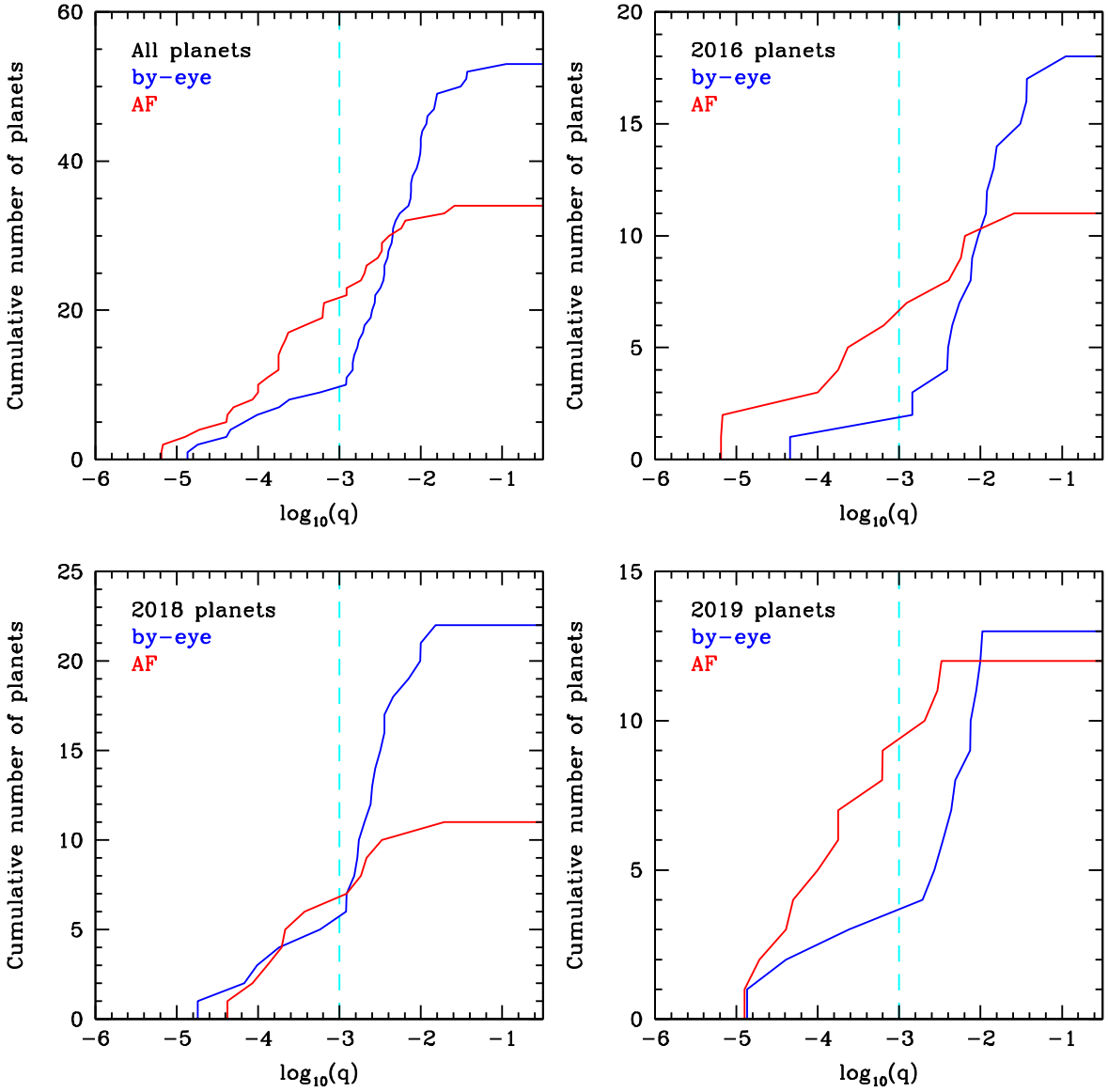

Figure 19. Cumulative number of planets discovered by the AF and eye as a function of $\log_{10}(q)$. We present 2016, 2018, and 2019 cases that have finished the systematic search for both prime and subprime fields.

by-eye searches. This fact clearly shows the importance of our systematic search to building a complete microlensing planet sample.

Acknowledgments

This research has made use of the KMTNet system operated by the Korea Astronomy and Space Science Institute (KASI) at three host sites of CTIO in Chile, SAAO in South Africa, and SSO in Australia. Data transfer from the host site to KASI was supported by the Korea Research Environment Open NETwork (KREONET). This research was supported by KASI under the R&D program (project No. 2023-1-832-03) supervised by the Ministry of Science and ICT. The MOA project is supported by JSPS KAKENHI grant Nos. JP24253004, JP26247023, JP16H06287, and JP22H00153. J.C.Y. and I.-G.S. acknowledge support from N.S.F grant No. AST-2108414. Work by C.H. was supported by the grants of National Research Foundation of Korea (2019R1A2C2085965 and 2020R1A4A2002885). Y.S. acknowledges support from BSF grant No. 2020740. W.Z. and H.Y. acknowledge support by the National Natural Science Foundation of China (grant No. 12133005). W.Z. acknowledges the support from the Harvard-Smithsonian Center for Astrophysics through the CfA Fellowship. The computations in this paper were conducted on the Smithsonian High Performance Cluster (SI/HPC), Smithsonian Institution (https://doi.org/10.25572/SIHPC). This research has made use of the NASA Exoplanet Archive, which is operated by the California Institute of Technology, under contract with the National Aeronautics and Space Administration under the Exoplanet Exploration Program.

Appendix
Nonplanetary Events

From the preliminary analysis using the pipeline data sets, we find that some events in the 2016 subprime fields have the potential to be caused by planetary lens systems (i.e., $q < 0.06$). However, based on the detailed analysis using the TLC data sets, we reveal that these events were caused by binary-lens systems.

The events cannot satisfy our criteria (i.e., no competing planetary solutions having $q < 0.03$ and $\Delta\chi^2 < 10.0$). Although the scientific importance is low for these events, we briefly document these binary-lens events for the record. This documentation will be helpful to avoid redundant efforts for planet searches using the KMTNet data archive. In Table 1, we list these nonplanetary events with their observational information.

A.1. OGLE-2016-BLG-0620

The overall shape of the light curve of OGLE-2016-BLG-0620 is a 1L1S-like feature. However, the 1L1S model exhibits residuals at the rising part of the left wing and around the peak. We find that these systematic residuals can be explained by the 2L1S interpretation, which gives $\Delta\chi^2 = 613.2$ between 1L1S and 2L1S models. The best-fit 2L1S model has $(s,\ q) = (2.449 \pm 0.050,\ 0.208 \pm 0.013)$, which indicates that the lens is a binary system. We also find a planet-like model (i.e., $q = 0.027 \pm 0.004$). However, this case is worse than the best fit by $\Delta\chi^2 = 30.7$, which does not satisfy our criterion (i.e., $\Delta\chi^2 < 10.0$). Thus, we conclude that OGLE-2016-BLG-0620 was caused by the binary rather than a planetary system.

A.2. KMT-2016-BLG-0913

The light curve of KMT-2016-BLG-0913 shows an apparent anomaly at the peak. We find the best-fit 2L1S model has $(s, q) = (2.492 \pm 0.067, 0.823 \pm 0.082)$. The best-fit model indicates that the lens system consists of binary stars. We check possible planetary models. We find two possible cases with $(s, q) = (1.328 \pm 0.032, 0.044 \pm 0.008)$, and $(s, q) = (0.700 \pm 0.009,\ 0.032 \pm 0.004)$. However, both cases are disfavored by $\Delta\chi^2 = 104.5$ and 116.7. Furthermore, the mass ratios of both cases do not satisfy our criterion. Thus, we conclude that KMT-2016-BLG-0913 was caused by a binary-lens system.

A.3. OGLE-2016-BLG-1432

The light curve of OGLE-2016-BLG-1432 shows an asymmetric feature. This anomaly can be explained by a 2L1S model with $(s, q) = (1.423 \pm 0.074, 0.257 \pm 0.063)$. The best-fit model indicates the lens is a binary-lens system. We also find a planetary model having $(s,\ q) = (1.603 \pm 0.056, (69.475 \pm 29.048) \times 10^{-4})$. However, the planetary case is disfavored by $\Delta\chi^2 = 78.1$. Thus, we conclude that OGLE-2016-BLG-1432 was caused by a binary.

A.4. KMT-2016-BLG-1222

The light curve of KMT-2016-BLG-1222 shows a clear anomaly at the peak. We find that the 2L1S interpretation can explain the anomaly. The best-fit solution with $(s,\ q) = (1.926 \pm 0.117,\ 0.113 \pm 0.024)$ indicates the lens is a binary. We also find a degenerate solution caused by the well-known close/wide degeneracy. This close solution with $(s,\ q) = (0.584 \pm 0.027,\ 0.088 \pm 0.017)$ has only $\Delta\chi^2 = 1.28$, so the degeneracy cannot be resolved. But, the close solution also indicates the lens is a binary. In addition, we find that there is no possible model having $q < 0.03$ based on the detailed analysis using the TLC data sets. Thus, we conclude that KMT-2016-BLG-1222 was caused by the binary.

A.5. OGLE-2016-BLG-1844

The light curve of OGLE-2016-BLG-1844 exhibits two bump-shaped anomalies at the peak. The anomaly can be described by 2L1S models with $(s,\ q) = (4.062 \pm 0.413,\ 0.313 \pm 0.088)$, or $(s,\ q) = (0.337 \pm 0.028,\ 0.171 \pm 0.034)$ corresponding to the s_+ or s_- cases, respectively. The degeneracy between the $s_\pm$ solutions cannot be resolved (i.e., $\Delta\chi^2 = 0.7$). Both $s_\pm$ cases indicate the lens is a binary system. We find possible planetary cases (i.e., $q \sim (38 \pm 5) \times 10^{-4}$) with s_+ ($s = 1.289 \pm 0.027$), and s_- ($s = 0.761 \pm 0.015$), but they are disfavored by $\Delta\chi^2 = 61.7$ and 62.1, respectively. Thus, we conclude that OGLE-2016-BLG-1844 was caused by a binary-lens system.

A.6. KMT-2016-BLG-1425

The light curve of KMT-2016-BLG-1425 shows an apparent bump near the peak. The anomaly can be described by a 2L1S model with $(s, q) = (1.169 \pm 0.057, 0.314 \pm 0.056)$ (the best-fit model). We find an alternative planetary model having $(s,\ q) = (1.279 \pm 0.062,\ 0.017 \pm 0.012)$. However, this case is disfavored by $\Delta\chi^2 = 17.7$, which does not satisfy our criterion (i.e., $\Delta\chi^2 < 10.0$). Thus, we conclude that OGLE-2016-BLG-0882 was caused by a binary-lens system.

A.7. OGLE-2016-BLG-0982

The light curve of OGLE-2016-BLG-0982 shows a clear bump-shaped anomaly near the peak. We find the best-fit solution has $(s,\ q) = (1.989 \pm 0.086,\ 0.660 \pm 0.090)$, which indicates the lens is a binary system. There are no possible planetary cases (i.e., $q < 0.03$). Among the competing solutions, the lowest q value is 0.083 ± 0.011, which is disfavored by $\Delta\chi^2 = 16.7$. Thus, we conclude that OGLE-2016-BLG-0982 was caused by a binary system.

A.8. OGLE-2016-BLG-1517

The light curve of OGLE-2016-BLG-1517 shows asymmetric deviations from the 1L1S fitting. The anomaly can be explained by the 2L1S models with $(s,\ q) = (3.259 \pm 0.103,\ 0.460 \pm 0.083)$. The best-fit solution indicates the lens is a binary. We have checked for possible planetary cases. However, we find that the model having the lowest q value (i.e., $q = 0.014 \pm 0.002$) is disfavored by $\Delta\chi^2 = 60.0$. Thus, we conclude that OGLE-2016-BLG-1517 was caused by a binary-lens system.

A.9. OGLE-2016-BLG-1258

OGLE-2016-BLG-1258 is a low-magnification event with a bump at the peak. The anomaly can be described by 2L1S models with $(s,\ q) = (0.573 \pm 0.012,\ 0.192 \pm 0.031)$, and $(s,\ q) = (2.002 \pm 0.085,\ 0.161 \pm 0.062)$ corresponding to the s_- and s_+ cases, respectively. The s_- case shows better fits than the s_+ case by $\Delta\chi^2 = 7.2$. Both solutions imply that the lens is a binary system. We find a possible planetary model ($q = 0.011 \pm 0.003$), which is disfavored by $\Delta\chi^2 = 27.4$. This planetary case is rejected based on our criterion. Thus, we conclude that OGLE-2016-BLG-1258 was caused by a binary-lens system.

A.10. KMT-2016-BLG-2256

The light curve of KMT-2016-BLG-2256 exhibits a bump-like anomaly, which is sparsely covered by KMTC only. The anomaly can be explained by both $s_{\pm}$ models with $(s, q) = (0.580 \pm 0.043, 0.629 \pm 0.197)$, and $(s, q) = (3.937 \pm 0.292, 0.360 \pm 0.410)$ corresponding to the s_- and s_+ cases, respectively. Although the $s_{\pm}$ cases cannot be resolved (i.e., $\Delta\chi^2 = 1.5$), both cases indicate that the lens is a binary system. We find that there is no competing planetary solution. The lowest q model (i.e., $q = 0.029 \pm 0.005$) is disfavored by $\Delta\chi^2 = 47.9$, which is clearly rejected based on our criterion. Thus, we conclude that KMT-2016-BLG-2256 was caused by a binary-lens system.

A.11. KMT-2016-BLG-2331

The light curve of KMT-2016-BLG-2331 shows a bump at the peak, which is sparsely covered. The anomaly can be described by both 2L1S models with $(s, q) = (0.317 \pm 0.025, 0.280 \pm 0.081)$, and $(s, q) = (5.014 \pm 0.646, 0.478 \pm 0.289)$ corresponding to the s_- and s_+ cases, respectively ($\Delta\chi^2 = 2.7$). Both $s_{\pm}$ cases indicate the lens is a binary. We find a possible planetary model having $q = (92.366 \pm 14.168) \times 10^{-4}$. However, this planet case is disfavored by $\Delta\chi^2 = 57.5$, which is clearly rejected based on our criterion. Thus, we conclude that KMT-2016-BLG-2331 was caused by a binary-lens system.

ORCID iDs

In-Gu Shin https://orcid.org/0000-0002-4355-9838
Jennifer C. Yee https://orcid.org/0000-0001-9481-7123
Weicheng Zang https://orcid.org/0000-0001-6000-3463
Cheongho Han https://orcid.org/0000-0002-2641-9964
Hongjing Yang https://orcid.org/0000-0003-0626-8465
Chung-Uk Lee https://orcid.org/0000-0003-0043-3925
Andrzej Udalski https://orcid.org/0000-0001-5207-5619
Takahiro Sumi https://orcid.org/0000-0002-4035-5012
Michael D. Albrow https://orcid.org/0000-0003-3316-4012
Sun-Ju Chung https://orcid.org/0000-0001-6285-4528
Yossi Shvartzvald https://orcid.org/0000-0003-1525-5041
Michał K. Szymański https://orcid.org/0000-0002-0548-8995
Jan Skowron https://orcid.org/0000-0002-2335-1730
Radosław Poleski https://orcid.org/0000-0002-9245-6368
Igor Soszyński https://orcid.org/0000-0002-7777-0842
Paweł Pietrukowicz https://orcid.org/0000-0002-2339-5899
Szymon Kozłowski https://orcid.org/0000-0003-4084-880X
Krzysztof A. Rybicki https://orcid.org/0000-0002-9326-9329
Patryk Iwanek https://orcid.org/0000-0002-6212-7221
Krzysztof Ulaczyk https://orcid.org/0000-0001-6364-408X
Marcin Wrona https://orcid.org/0000-0002-3051-274X
Mariusz Gromadzki https://orcid.org/0000-0002-1650-1518
David P. Bennett https://orcid.org/0000-0001-8043-8413
Akihiko Fukui https://orcid.org/0000-0002-4909-5763
Yuki Hirao https://orcid.org/0000-0003-4776-8618
Yoshitaka Itow https://orcid.org/0000-0002-8198-1968
Naoki Koshimoto https://orcid.org/0000-0003-2302-9562
Yutaka Matsubara https://orcid.org/0000-0002-9629-4810
Shota Miyazaki https://orcid.org/0000-0001-9818-1513
Yasushi Muraki https://orcid.org/0000-0003-1978-2092
Kansuke Nunota https://orcid.org/0009-0005-3414-455X
Greg Olmschenk https://orcid.org/0000-0001-8472-2219
Yuki Satoh https://orcid.org/0000-0002-1228-4122
Daisuke Suzuki https://orcid.org/0000-0002-5843-9433

References

Alard, C., & Lupton, R. H. 1998, ApJ, 503, 325
Albrow, M. D., Horne, K., Bramich, D. M., et al. 2009, MNRAS, 397, 2099
Bennett, D. P., Bond, I. A., Udalski, A., et al. 2008, ApJ, 684, 663
Bond, I. A., Abe, F., Dodd, R. J., et al. 2001, MNRAS, 327, 868
Bond, I. A., Bennett, D. P., Sumi, T., et al. 2017, MNRAS, 469, 2434
Calchi Novati, S., Suzuki, D., Udalski, A., et al. 2019, AJ, 157, 121
Chang, K., & Refsdal, S. 1979, Natur, 282, 561
Clanton, C., & Gaudi, B. S. 2014a, ApJ, 791, 90
Clanton, C., & Gaudi, B. S. 2014b, ApJ, 791, 91
Gaudi, B. S. 1998, ApJ, 506, 533
Gould, A. 1992, ApJ, 392, 442
Gould, A. 2022, arXiv:2209.12501
Gould, A., Han, C., Zang, W., et al. 2022, A&A, 664, A13
Gould, A., Shvartzvald, Y., Zhang, J., et al. 2023, AJ, 166, 145
Griest, K., & Safizadeh, N. 1998, ApJ, 500, 37
Han, C., Bond, I. A., Gould, A., et al. 2018, AJ, 156, 226
Han, C., Udalsk, A., Gould, A., et al. 2020a, AJ, 159, 91
Han, C., Udalski, A., Gould, A., et al. 2017a, AJ, 154, 133
Han, C., Udalski, A., Gould, A., et al. 2017b, AJ, 154, 223
Han, C., Udalski, A., Kim, D., et al. 2020b, A&A, 642, A110
Holtzman, J. A., Watson, A. M., Baum, W. A., et al. 1998, AJ, 115, 1946
Hwang, K.-H., Ryu, Y.-H., Kim, H.-W., et al. 2019, AJ, 157, 23
Hwang, K.-H., Udalski, A., Shvartzvald, Y., et al. 2018, AJ, 155, 20
Hwang, K.-H., Zang, W., Gould, A., et al. 2022, AJ, 163, 43
Ida, S., & Lin, D. N. C. 2005, ApJ, 626, 1045
Jiang, G., DePoy, D. L., Gal-Yam, A., et al. 2004, ApJ, 617, 1307
Jung, Y. K., Hwang, K.-H., Ryu, Y.-H., et al. 2018, AJ, 156, 208
Jung, Y. K., Zang, W., Han, C., et al. 2022, AJ, 164, 262
Jung, Y. K., Zang, W., Wang, H., et al. 2023, AJ, 165, 226
Kennedy, G. M., & Kenyon, S. J. 2008, ApJ, 673, 502
Kim, D.-J., Kim, H.-W., Hwang, K.-H., et al. 2018, AJ, 155, 76
Kim, S.-L., Lee, C.-U., Park, B.-G., et al. 2016, JKAS, 49, 37
Koshimoto, N., Shvartzvald, Y., Bennett, D. P., et al. 2017, AJ, 154, 3
Mróz, P., Han, C., Udalski, A., et al. 2017, AJ, 153, 143
Poindexter, S., Afonso, C., Bennett, D. P., et al. 2005, ApJ, 633, 914
Ryu, Y.-H., Hwang, K.-H., Gould, A., et al. 2021, AJ, 162, 96
Ryu, Y.-H., Kil Jung, Y., Yang, H., et al. 2022, AJ, 164, 180
Ryu, Y.-H., Udalski, A., Yee, J. C., et al. 2024, AJ, 167, 88
Ryu, Y.-H., Yee, J. C., Udalski, A., et al. 2018, AJ, 155, 40
Shin, I.-G., Ryu, Y.-H., Yee, J. C., et al. 2019, AJ, 157, 146
Shin, I.-G., Yee, J. C., Gould, A., et al. 2023a, AJ, 165, 8
Shin, I.-G., Yee, J. C., Hwang, K.-H., et al. 2022, AJ, 163, 254
Shin, I.-G., Yee, J. C., Zang, W., et al. 2023b, AJ, 166, 104
Shvartzvald, Y., Maoz, D., Udalski, A., et al. 2016, MNRAS, 457, 4089
Shvartzvald, Y., Yee, J. C., Calchi Novati, S., et al. 2017, ApJL, 840, L3
Smith, M. C., Mao, S., & Paczyński, B. 2003, MNRAS, 339, 925
Sumi, T., Abe, F., Bond, I. A., et al. 2003, ApJ, 591, 204
Szymański, M. K., Udalski, A., Soszyński, I., et al. 2011, AcA, 61, 83
Tomaney, A. B., & Crotts, A. P. S. 1996, AJ, 112, 2872
Udalski, A., Szymanski, M., Kaluzny, J., et al. 1994, AcA, 44, 227
Udalski, A., Szymański, M. K., & Szymański, G. 2015, AcA, 65, 1
Wang, H., Zang, W., Zhu, W., et al. 2022, MNRAS, 510, 1778
Wozniak, P. R. 2000, AcA, 50, 421
Yang, H., Yee, J. C., Hwang, K.-H., et al. 2024, MNRAS, 528, 11
Yang, H., Zhang, X., Hwang, K.-H., et al. 2020, AJ, 159, 98
Yee, J. C., Shvartzvald, Y., Gal-Yam, A., et al. 2012, ApJ, 755, 102
Yoo, J., DePoy, D. L., Gal-Yam, A., et al. 2004, ApJ, 603, 139
Zang, W., Hwang, K.-H., Kim, H.-W., et al. 2018, AJ, 156, 236
Zang, W., Hwang, K.-H., Udalski, A., et al. 2021, AJ, 162, 163
Zang, W., Jung, Y. K., Yang, H., et al. 2023, AJ, 165, 103
Zang, W., Jung, Y. K., Yee, J. C., et al. 2024, Sci, submitted
Zang, W., Yang, H., Han, C., et al. 2022, MNRAS, 515, 928